MOX-Report No. 06/2016

Anisotropic mesh adaptation for the generalized Ambrosio-Tortorelli functional with application to brittle fracture

Micheletti, S.; Perotto, S.; Signorini, M.

MOX, Dipartimento di Matematica
Politecnico di Milano, Via Bonardi 9 - 20133 Milano (Italy)

mox-dmat@polimi.it http://mox.polimi.it

Anisotropic mesh adaptation for the generalized Ambrosio-Tortorelli functional with application to brittle fracture

Stefano Micheletti, Simona Perotto and Marianna Signorini

February 2, 2016

MOX– Modellistica e Calcolo Scientifico
Dipartimento di Matematica
Politecnico di Milano
Piazza L. da Vinci 32, I-20133 Milano, Italy
{stefano.micheletti,simona.perotto,marianna.signorini}@polimi.it

Keywords: Adaptive finite element method, AmbrosioTortorelli functional, brittle fracture, anisotropic mesh adaptation, a posteriori error estimator

Abstract

Quasi-static crack propagation in brittle materials is modeled via the Ambrosio-Tortorelli approximation [7]. The crack is modeled by a smooth phase-field, defined on the whole computational domain. Since the crack is confined to a thin layer, the employment of anisotropic adapted grids is shown to be a really effective tool in containing computational costs. We extend the error analysis in [3, 4, 5] to the generalized Ambrosio-Tortorelli functional introduced in [8], where a unified framework for several elasticity laws is dealt with as well as a non-convex fracture energy can be accommodated. After deriving an anisotropic a posteriori error estimator, we devise an algorithm which alternates optimization and mesh adaptation. Both anti-plane and plane-strain configurations are numerically checked.

1 Introduction

Modeling crack propagation in brittle materials is an area of great interest in different areas, such as in materials science, solid mechanics or geoscience.

A very accurate setting to model crack propagation is provided by the Francfort-Marigo theory, introduced in [18]. The main strength of this approach is the capability to predict the crack path without any a priori knowledge [12, 13, 17]. Nevertheless, the Francfort-Marigo model requires minimizing a highly irregular functional (also known as the Mumford-Shah functional in image segmentation) which is very complex to be approximated numerically.

Therefore, several methods have been proposed in the literature to approximate the Francfort-Marigo model and to end up with a more handy computable approximation. A very well-known approach in this context is the Ambrosio-Tortorelli approximation [1, 2]. The fracture propagation is described in terms of a free-discontinuity problem, through the introduction of a dedicated phase-field variable. The main challenge of a phase-field approach is represented by the sharp detection of the transition region between fractured and unfractured material. With a view to a finite element discretization, this may represents a numerical obstacle since a very fine mesh is demanded in a neighborhood of the crack, whose location is unknown and varying in time.

Mesh adaptation represents an effective answer to this issue, since it allows one to refine the mesh only where strictly necessary, i.e., along the crack path. In [7], for instance, the authors provide a first theoretically sound attempt in such a direction by introducing an isotropic mesh adaptation procedure driven by an a posteriori error estimator. This analysis is extended to an anisotropic setting in [3, 4, 5], where the well-established benefits of anisotropic meshes are successively assessed. In [8], a generalized Ambrosio-Tortorelli functional is provided to include more general elastic laws and energy contributions and discretized via isotropic adaptive finite elements.

The new contribution of this work is the extension of the anisotropic a posteriori error analysis in [3, 4, 5] to the generalized Ambrosio-Tortorelli functional, thus including a possible non-convex dependence of the functional on the phase-field variable. This requires a careful modification of the optimization procedure. The new adaptive algorithm is verified on some benchmark test cases by checking the consistency with respect to the results in the literature and emphasizing the benefits led by an anisotropic mesh adaptation.

The paper is organized as follows. Section 2 introduces the generalized Ambrosio-Tortorelli functional in the original formulation and in a modified version where the physical constraints of the problem are weakly imposed by penalty. Section 3 represents the main core of this work where the anisotropic a posteriori error analysis is carried out. The Optimize-while-Adapt algorithm is set in Section 4 together with all the practical numerical details. In Section 5, we focus on the numerical assessment by considering anti-plane and plane-strain configurations. Finally, some conclusions are drawn in the last section.

2 The generalized Ambrosio-Tortorelli functional

The goal of the proposed generalization is twofold. On the one hand, we provide a unique framework combining the plane and anti-plane linear elasticity tackled separately in [5, 3] and [4], respectively; on the other hand, we consider the generalized Ambrosio-Tortorelli (gAT) functional proposed in [8]. As the standard Ambrosio-Tortorelli functional has been introduced to Γ-approximate the Francfort-Marigo (FM) energy functional, according to [8], we may assume that gAT still Γ-converges to FM.

With a view to the first issue, we introduce some new notation to embrace simultaneously vector and tensor quantities.

Definition 2.1 *We introduce three multiplication operators:*

$$Z \diamond W = \begin{cases} Z \cdot W & \textit{if } Z, W \in \mathbb{R}^2 \\ Z : W & \textit{if } Z, W \in \mathbb{R}^{2\times 2}, \end{cases}$$

where $\cdot$ and $:$ denote the standard inner product in $\mathbb{R}^2$ and $\mathbb{R}^{2\times 2}$, respectively;

$$Z \odot W = \begin{cases} ZW & \textit{if } Z, W \in \mathbb{R} \\ Z \cdot W & \textit{if } Z, W \in \mathbb{R}^2; \end{cases}$$

$$Z \times W = \begin{cases} Z \otimes W & \textit{if } Z, W \in \mathbb{R}^2 \\ ZW & \textit{if } Z \in \mathbb{R}, W \in \mathbb{R}^2, \end{cases}$$

where $\otimes$ denotes the Kronecker product between vectors.

We now focus on the second issue. The gAT functional depends on two functions, F,$G \in \mathcal{C}^3([0,1])$, such that F is an increasing function with $F(0) = 0$ and $F(1) = 1$, G is non-negative with $G(z) = 0$ if and only if $z = 1$. It is defined by

$$J_\varepsilon(\mathbf{u}, v) = \int_\Omega (F(v) + \eta) A\nabla\mathbf{u} \diamond \nabla\mathbf{u}\, d\mathbf{x} + \mathcal{K} \int_\Omega (\varepsilon^{-1} G(v) + \varepsilon|\nabla v|^2)\, d\mathbf{x}, \tag{1}$$

where $\Omega \subset \mathbb{R}^2$ is a polygonal domain, $\mathbf{u} : \Omega \to \mathbb{R}^n$ for $n = 1, 2$, and $v : \Omega \to [0,1]$ are the displacement and the phase-field, respectively, $0 < \eta \ll \varepsilon \ll 1$ are suitable regularization constants, A is the elasticity tensor and $\mathcal{K}$ is the fracture toughness of the body. In particular, the displacement $\mathbf{u}$ is assigned over a subset $\Omega_D \subset \Omega$ through the vector field $\mathbf{g} : \Omega \times [0,T] \to \mathbb{R}^n$, with

$$\mathbf{g}(t) = \begin{cases} \mathbf{g}_D(t) & \text{on } \Omega_D,\ t \in [0,T] \\ 0 & \text{otherwise}, \end{cases} \tag{2}$$

T being the final time and where the dependence on $\mathbf{x} = (x_1, x_2)^T$ is understood; the phase-field v is a smoothed crack path indicator, such that

$$v(\mathbf{x}) = \begin{cases} 0 & \text{if the material is damaged at } \mathbf{x} \\ 1 & \text{otherwise;} \end{cases}$$

the elasticity tensor A is assumed symmetric (major symmetries) and frame indifferent (minor symmetries). Due to these symmetries, we can assume that, for $Z = \{Z_i\}_{i=1}^n : \Omega \to \mathbb{R}^n$, the gradient is defined by $\left(\nabla Z\right)_{ji} = \partial Z_i / \partial x_j$, with $j = 1, 2$, $i = 1, \dots, n$, where it is understood that, for $n = 1$, $Z_1 = Z$.

From a physical viewpoint, functions F and G weight the contributions of the elastic and of the crack energy to the total one, so that the total energy coincides with the elastic one where the material is unbroken, whereas it reduces to the crack energy where the material is completely damaged, up to the η-contribution. The gAT functional recovers the classical Ambrosio-Tortorelli functional when $F(v) = v^2$ and $G(v) = (1 - v)^2/4$ [6, 19].

Independently of the particular choice for F and G, the variational model describes a quasi-static evolution of the crack propagation. Thus, we discretize the problem in time and define a new minimization problem, associated with each time level. For this purpose, we subdivide the time window $[0, T]$ by the partition $0 = t_0 < t_1 < \cdots < t_N = T$, so that, at each time step, we are led to find the pair $(\mathbf{u}(t_k), v(t_k)) \in H^1(\Omega; \mathbb{R}^n) \times H^1(\Omega; [0, 1])$ satisfying $\mathbf{u}(t_k)|_{\Omega_D} = \mathbf{g}_D(t_k)$ and, for each $k > 0$, the irreversibility condition $v(t_k) \leq v(t_{k-1})$ in CR_{k-1}, where $CR_{k-1} = \{\mathbf{x} \in \Omega : v(t_{k-1}) < \texttt{CRTOL}\}$ describes the damaged area at t_{k-1} up to the tolerance CRTOL. The condition on v ensures that, after a part of the body is damaged, it cannot heal.

The minimization problem can thus be formalized as: find $(\mathbf{u}, v) \in H^1_g(\Omega) \times K$ such that

$$(\mathbf{u}, v) \in \operatorname{argmin}\{J_\varepsilon(\hat{\mathbf{u}}, \hat{v}) : \hat{\mathbf{u}} \in H^1_g(\Omega), \hat{v} \in K\}, \tag{3}$$

where $H^1_g(\Omega) = \{\mathbf{u} \in H^1(\Omega; \mathbb{R}^n) : \mathbf{u} = \mathbf{g}_D(t_k) \text{ on } \Omega_D\}$, $K = \{v \in H^1(\Omega; \mathbb{R}) : 0 \leq v \leq \chi \text{ a.e. in} \Omega\}$, where $\chi \in H^1(\Omega; [0, 1])$ is equal to $v(t_{k-1})$ in CR_{k-1} and increases continuously to 1 away from CR_{k-1} [8].

2.1 Penalizing the gAT functional

Following [3, 4, 5], we enforce in a weak sense the constraint on the assigned displacement on Ω_D and the irreversibility condition. Thus, at each time step, we minimize the modified cost functional

$$J(\mathbf{u}, v) = \frac{1}{2} J_\varepsilon(\mathbf{u}, v) + \frac{1}{2\gamma_A} \int_{\Omega_D} |\mathbf{u} - \mathbf{g}_D(t_k)|^2 \, d\mathbf{x} + \frac{1}{2\gamma_B} \int_{CR_{k-1}} v^2 \, d\mathbf{x}, \tag{4}$$

where γ_A and γ_B are the penalty constants. As a consequence, problem (3) is reformulated as: find $(\mathbf{u}, v) \in H^1(\Omega; \mathbb{R}^n) \times H^1(\Omega; [0, 1])$ such that

$$(\mathbf{u}, v) \in \operatorname{argmin}\{J(\hat{\mathbf{u}}, \hat{v}) : \hat{\mathbf{u}} \in H^1(\Omega; \mathbb{R}^n), \hat{v} \in H^1(\Omega; [0, 1])\}. \tag{5}$$

The two minimization problems (5) and (3) are related by the property that the minimizers of (5) converge to the minimizers of (3) for γ_A, $\gamma_B \to 0$, since the penalization constraints are continuous, convex and always non-negative (see [11]).

To solve the minimization problem (5), we introduce the Gâteaux derivatives of gAT functional J. In particular, by mimicking Proposition 2.1 in [8], we have that functional J is Gâteaux differentiable in $V = H^1(\Omega;\mathbb{R}^n) \times (H^1(\Omega;[0,1]) \cap L^\infty(\Omega))$. In more detail, the Gâteaux derivative of J at $(\mathbf{u}, v) \in V$ along the direction $(\boldsymbol{\phi}, \psi) \in V$ is given by

$$J'(\mathbf{u}, v; \boldsymbol{\phi}, \psi) = a(v; \mathbf{u}, \boldsymbol{\phi}) + b(\mathbf{u}; v, \psi), \tag{6}$$

where

$$\begin{aligned} a(v; \mathbf{u}, \boldsymbol{\phi}) &= \partial_{\mathbf{u}} J(v; \mathbf{u}, \boldsymbol{\phi}) \\ &= \int_\Omega (F(v) + \eta) A \nabla \mathbf{u} \diamond \nabla \boldsymbol{\phi} \, d\mathbf{x} + \frac{1}{\gamma_A} \int_{\Omega_D} (\mathbf{u} - \mathbf{g}_D(t_k)) \odot \boldsymbol{\phi} \, d\mathbf{x} \end{aligned} \tag{7}$$

and

$$\begin{aligned} b(\mathbf{u}; v, \psi) &= \partial_v J(\mathbf{u}; v, \psi) \\ &= \frac{1}{2} \int_\Omega F'(v) A \nabla \mathbf{u} \diamond \nabla \mathbf{u} \, \psi \, d\mathbf{x} \\ &+ \frac{\mathcal{K}}{2} \int_\Omega (\varepsilon^{-1} G'(v) \psi + 2\varepsilon \nabla v \cdot \nabla \psi) \, d\mathbf{x} + \frac{1}{\gamma_B} \int_{CR_{k-1}} v \psi \, d\mathbf{x}. \end{aligned} \tag{8}$$

Solving (5) is equivalent to computing the critical points $(\mathbf{u}, v) \in V$ which satisfy the variational equality and inequality:

$$\begin{aligned} \partial_{\mathbf{u}} J(v; \mathbf{u}, \boldsymbol{\phi}) = 0 \quad & \forall \boldsymbol{\phi} \in H^1(\Omega; \mathbb{R}^n) \\ \partial_v J(\mathbf{u}; v, v - \psi) \leq 0 \quad & \forall \psi \in H^1(\Omega; [0,1]) \cap L^\infty(\Omega). \end{aligned} \tag{9}$$

2.2 Discretization of the minimization problem

Following [3, 4, 5], we move to the discrete setting. For the present purposes, we introduce a family $\{\mathcal{T}_h\}$ of conforming meshes of $\bar{\Omega}$, by denoting with X_h the associated space of continuous piecewise linear finite elements [9]. We approximate the assigned displacement in (2) at $t = t_k$ by $\mathbf{g}_h(t_k) = \{g_{h,i}(t_k)\}_{i=1}^n \in [X_h]^n$ such that

$$\int_{\Omega_D} \mathbf{g}_h(t_k) \odot \mathbf{w}_h \, d\mathbf{x} = \int_{\Omega_D} \mathbf{g}_D(t_k) \odot \mathbf{w}_h \, d\mathbf{x} \quad \forall \mathbf{w}_h \in [X_h]^n.$$

The discrete version of (5) reads: find $\mathbf{u}_h = \{u_{h,i}\}_{i=1}^n \in [X_h]^n$ and $v_h \in X_h \cap H^1(\Omega;[0,1])$ such that

$$(\mathbf{u}_h, v_h) \in \operatorname{argmin}\{J_h(\hat{\mathbf{u}}_h, \hat{v}_h) : \hat{\mathbf{u}}_h \in [X_h]^n, \hat{v}_h \in X_h \cap H^1(\Omega;[0,1]), \tag{10}$$

where

$$
\begin{aligned}
J_h(\mathbf{u}_h, v_h) = &\frac{1}{2}\int_\Omega (P_h(F(v_h)) + \eta) A\nabla\mathbf{u}_h \diamond \nabla\mathbf{u}_h \, d\mathbf{x} \\
&+ \frac{\mathcal{K}}{2}\int_\Omega \left(\varepsilon^{-1} P_h(G(v_h)) + \varepsilon|\nabla v_h|^2\right) \, d\mathbf{x} \\
&+ \frac{1}{2\gamma_A}\sum_{i=1}^{n}\int_{\Omega_D} P_h(u_{h,i} - g_{h,i}(t_k))^2 \, d\mathbf{x} + \frac{1}{2\gamma_B}\int_{CR_{k-1}} P_h(v_h^2) \, d\mathbf{x},
\end{aligned}
$$

$P_h : \mathcal{C}^0(\bar{\Omega}) \to X_h$ being the Lagrange interpolation operator associated with X_h. The introduction of P_h is motivated by the consistency with the standard discrete Ambrosio-Tortorelli functional in [3, 4, 5], where the constraint $0 \le v_h \le 1$ is automatically guaranteed. In the general case of the gAT functional, this last constraint has to be enforced directly during the optimization procedure.

We replicate the procedure in (6)-(9) in the discrete setting. In particular, (6) is replaced by

$$
J_h'(\mathbf{u}_h, v_h; \boldsymbol{\phi}_h, \psi_h) = a_h(v_h; \mathbf{u}_h, \boldsymbol{\phi}_h) + b_h(\mathbf{u}_h; v_h, \psi_h),
$$

where

$$
\begin{aligned}
a_h(v_h; \mathbf{u}_h, \boldsymbol{\phi}_h) &= \partial_{\mathbf{u}_h} J_h(v_h; \mathbf{u}_h, \boldsymbol{\phi}_h) \\
&= \int_\Omega (P_h(F(v_h)) + \eta) A\nabla\mathbf{u}_h \diamond \nabla\boldsymbol{\phi}_h d\mathbf{x} \\
&+ \frac{1}{\gamma_A}\sum_{i=1}^{2}\int_{\Omega_D} P_h\left((u_{h,i} - g_{h,i}(t_k))\phi_{h,i}\right) \, d\mathbf{x}
\end{aligned}
\tag{11}
$$

with $\boldsymbol{\phi}_h = \{\phi_{h,i}\}_{i=1}^n$, and

$$
\begin{aligned}
b_h(\mathbf{u}_h; v_h, \psi_h) &= \partial_{v_h} J_h(\mathbf{u}_h; v_h, \psi_h) \\
&= \frac{1}{2}\int_\Omega P_h(F'(v_h)\psi_h) A\nabla\mathbf{u}_h \diamond \nabla\mathbf{u}_h \, d\mathbf{x} + \frac{\mathcal{K}}{2}\int_\Omega (\varepsilon^{-1} P_h(G'(v_h)\psi_h) \\
&+ 2\varepsilon\nabla v_h \cdot \nabla\psi_h) \, d\mathbf{x} + \frac{1}{\gamma_B}\int_{CR_{k-1}} P_h(v_h\psi_h) \, d\mathbf{x}.
\end{aligned}
\tag{12}
$$

Thus, we are led computing the critical points $(\mathbf{u}_h, v_h) \in [X_h]^n \times X_h \cap H^1(\Omega; [0,1])$ of J_h that satisfy relations

$$
\begin{aligned}
\partial_{\mathbf{u}_h} J_h(v_h; \mathbf{u}_h, \boldsymbol{\phi}_h) = 0 \quad & \forall \boldsymbol{\phi}_h \in [X_h]^n \\
\partial_{v_h} J_h(\mathbf{u}_h; v_h, v_h - \psi_h) \le 0 \quad & \forall \psi_h \in X_h \cap H^1(\Omega; [0,1]).
\end{aligned}
\tag{13}
$$

3 Anisotropic a posteriori error analysis

This section provides the main theoretical contribution of this work. After a brief introduction on the anisotropic setting, we derive the a posteriori error estimator used to drive the mesh adaptation.

3.1 The anisotropic setting

We adopt the setting employed in [15, 22, 14, 23], where the anisotropic information is derived from the spectral properties of the standard affine map T_K from the reference triangle $\hat{K}$ to the generic element, K, of $\mathcal{T}_h$. Map $T_K : \hat{K} \to K$ is such that $\mathbf{x} = T_K(\hat{\mathbf{x}}) = M_K\hat{\mathbf{x}} + \mathbf{t}_K$, where $M_K \in \mathbb{R}^{2\times 2}$ is its Jacobian, $\mathbf{t}_K \in \mathbb{R}^2$ is the shift vector, $\mathbf{x} \in K$ and $\hat{\mathbf{x}} \in \hat{K}$ denote the generic point of the actual and the reference triangles. In particular, the reference element $\hat{K}$ is the equilateral triangle inscribed in the unit circle, as shown in Figure 1.

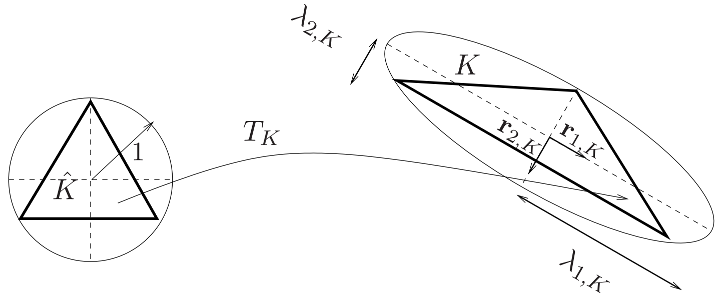

Figure 1: Geometric quantities associated with the map T_K

We compute the polar decomposition $M_K = B_K Z_K$ of the Jacobian matrix M_K to identify the rotation Z_K and the stretching B_K matrices which change the reference triangle $\hat{K}$ into K, where B_K is symmetric positive definite and Z_K is orthogonal. We successively perform the spectral decomposition of B_K as $B_K = R_K^T \Lambda_K R_K$, with $R_K^T = [\mathbf{r}_{1,K}, \mathbf{r}_{2,K}]$, $\Lambda_K = \mathrm{diag}(\lambda_{1,K}, \lambda_{2,K})$ and $\lambda_{1,K} \geq \lambda_{2,K} > 0$. In particular, the eigenvectors $\mathbf{r}_{i,K}$ identify the directions of the semi-axes of the ellipse circumscribing K, while the eigenvalues $\lambda_{i,K}$ measure the corresponding lengths (see Figure 1). The aspect ratio $s_K = \lambda_{1,K}/\lambda_{2,K} \geq 1$ quantifies the deformation of the element K, $s_K = 1$ identifying the undeformed case of an isotropic equilateral triangle.

To derive the a posteriori error estimator, we recall the anisotropic estimates for the Clément quasi-interpolant operator $\mathcal{C}_h : L^2(\Omega) \to X_h$. These estimates are proved in [10] for the isotropic case and generalized to an anisotropic setting in [15, 16].

Lemma 3.1 *Let $w \in H^1(\Omega)$, $\mathrm{diam}(T_K^{-1}(\Delta_K)) \leq C_\Delta$ and $\#\Delta_K \leq \mathcal{N}$, for some $\mathcal{N} \in \mathbb{N}$, where $\#\Delta_K$ denotes the cardinality of the patch $\Delta_K = \{T \in \mathcal{T}_h : T \cap K \neq \emptyset\}$ of the elements associated with K. Then, for any $K \in \mathcal{T}_h$, the* *following estimates hold*

$$
\begin{aligned}
\|w - \mathcal{C}_h(w)\|_{L^2(K)} &\leq C_1 \left[\sum_{j=1}^{2} \lambda_{j,K}^2 (\mathbf{r}_{j,K}^T G_{\Delta_K}(w) \mathbf{r}_{j,K}) \right]^{1/2}, \\
|w - \mathcal{C}_h(w)|_{H^1(K)} &\leq C_2 \frac{1}{\lambda_{2,K}} \left[\sum_{j=1}^{2} \lambda_{j,K}^2 (\mathbf{r}_{j,K}^T G_{\Delta_K}(w) \mathbf{r}_{j,K}) \right]^{1/2}, \\
\|w - \mathcal{C}_h(w)\|_{L^2(\partial K)} &\leq C_3 \left(\frac{h_K}{\lambda_{1,K}\lambda_{2,K}} \right)^{1/2} \left[\sum_{j=1}^{2} \lambda_{j,K}^2 (\mathbf{r}_{j,K}^T G_{\Delta_K}(w) \mathbf{r}_{j,K}) \right]^{1/2},
\end{aligned}
$$

for some constants $C_s = C_s(\mathcal{N}, C_\Delta)$, with $s = 1, 2, 3$, where $h_K = \mathrm{diam}(K)$ and $G_{\Delta_K}(w)$ is the 2-by-2 symmetric semipositive definite matrix with entries

$$
\big[G_{\Delta_K}(w)\big]_{ij} = \sum_{T \in \Delta_K} \int_T \frac{\partial w}{\partial x_i} \frac{\partial w}{\partial x_j} \, d\mathbf{x} \quad i, j = 1, 2.
$$

Moreover, we recall the following equivalence result between the $H^1(\Delta_K)$-seminorm and an anisotropic counterpart. The proof can be found in [21].

Lemma 3.2 *Let $w \in H^1(\Omega)$ and $K \in \mathcal{T}_h$. For any $\beta_1, \beta_2 > 0$, it holds*

$$
\min\{\beta_1, \beta_2\} \leq \frac{\displaystyle\sum_{i=1}^{2} \beta_i (\mathbf{r}_{i,K}^T G_{\Delta_K}(w) \mathbf{r}_{i,K})}{|w|_{H^1(\Delta_K)}^2} \leq \max\{\beta_1, \beta_2\}.
$$

3.2 The anisotropic a posteriori error estimator

We extend the a posteriori analysis in [3, 4, 5] to the gAT functional, by properly dealing with the general functions F and G. For the sake of simplicity, we replace the variational inequality in (13) with the constraint $\partial_{v_h} J_h(\mathbf{u}_h; v_h, \psi_h) = 0$, for any $\psi_h \in V_h$. This is essentially equivalent to assuming that the constraint on v_h reduces to the strict inequality $0 < v_h < 1$ in Ω, i.e., the upper and lower coincidence sets are empty.

We start by providing a technical result which links the multiplication operators introduced in Definition 2.1 and follows by a straightforward application of the Gauss theorem and some componentwise differential relations.

Lemma 3.3 *Let $v : \mathcal{D} \to \mathbb{R}$, $Z, W : \mathcal{D} \to \mathbb{R}^n$, $Y : \mathcal{D} \to \mathbb{R}^2$ be sufficiently regular functions with $\mathcal{D}$ a polygonal domain in $\mathbb{R}^2$. Then, it holds*

$$
\begin{aligned}
&\int_{\mathcal{D}} F(v) A\nabla Z \diamond \nabla W \, d\mathbf{x} = \int_{\partial\mathcal{D}} F(v) A\nabla Z \diamond (W \times \mathbf{n}) \, ds \\
&- \int_{\mathcal{D}} \Big[F'(v) A\nabla Z \diamond \big(W \times \nabla v\big) + F(v) \nabla \cdot \big(A\nabla Z\big) \odot W \Big] \, d\mathbf{x},
\end{aligned}
$$

where F and A are the same functions as in (1), $\mathbf{n}$ is the unit outward normal vector to $\partial\mathcal{D}$ and the divergence operator $\nabla\cdot$ is denoted by the same symbol for both vectors and tensors. Moreover, componentwise it holds

$$A\nabla Z \diamond \nabla W = \sum_{i=1}^{n} \big(A\nabla Z\big)_i \cdot \big(\nabla W\big)_i$$
$$A\nabla Z \diamond \big(W \times Y\big) = \sum_{i=1}^{n} \big(A\nabla Z\big)_i \cdot Y\, W_i,$$

with $Y = (Y_1, Y_2)^T$, and where $\big(\,\cdot\,\big)_i$ denotes the i-th column for tensors or the quantity itself for vectors.

Theorem 3.1 *Let $(\mathbf{u}_h, v_h) \in [X_h]^n \times X_h$ be a critical point of J_h. Then, for all $(\boldsymbol{\phi}, \psi) \in [H^1(\Omega)]^n \times H^1(\Omega)$, with $\boldsymbol{\phi} = \{\phi_i\}_{i=1}^n$, the following estimate holds:*

$$|J'(\mathbf{u}_h, v_h; \boldsymbol{\phi}, \psi)| \leq C \sum_{K\in\mathcal{T}_h} \left\{ \sum_{i=1}^{n} \rho^A_{i,K}(v_h, \mathbf{u}_h)\omega_K(\phi_i) + \rho^B_K(\mathbf{u}_h, v_h)\omega_K(\psi) \right\}, \quad (14)$$

where the weights are

$$\omega_K(z) = \left[\sum_{j=1}^{2} \lambda^2_{j,K} \left(\mathbf{r}^T_{j,K} G_{\Delta_K}(z)\mathbf{r}_{j,K}\right) \right]^{1/2} \qquad \forall z \in H^1(\Omega), \quad (15)$$

while the residual $\rho^A_{i,K}$, $i = 1, \dots, n$, and ρ^B_K are defined as

$$\begin{aligned}
\rho^A_{i,K}(v_h, \mathbf{u}_h) = {} & \big\|F'(v_h)(A\nabla\mathbf{u}_h)_i \cdot \nabla v_h + F(v_h)\nabla\cdot(A\nabla\mathbf{u}_h)_i\big\|_{L^2(K)} \\
& + \frac{1}{\lambda_{2,K}} \|F(v_h) - P_h(F(v_h))\|_{L^\infty(K)} \|(A\nabla\mathbf{u}_h)_i\|_{L^2(K)} \\
& + \frac{1}{2}\, \|[\![(A\nabla\mathbf{u}_h)_i]\!]\|_{L^\infty(\partial K)}\, \|F(v_h) + \eta\|_{L^2(\partial K)} \left(\frac{h_K}{\lambda_{1,K}\lambda_{2,K}}\right)^{1/2} \\
& + \frac{\delta_{K,\Omega_D}|K|^{1/2}h^2_K}{\lambda_{2,K}\gamma_A} |u_{h,i} - g_{h,i}(t_k)|_{W^{1,\infty}(K)} \\
& + \frac{\delta_{K,\Omega_D}}{\gamma_A} \Big(\|u_{h,i} - g_{h,i}(t_k)\|_{L^2(K)} + \|g_{h,i}(t_k) - g_i(t_k)\|_{L^2(K)} \Big),
\end{aligned}$$

$$\begin{aligned}
\rho^B_K(\mathbf{u}_h, v_h) = {} & \frac{1}{2}\, \big\|F'(v_h)A\nabla\mathbf{u}_h \diamond \nabla\mathbf{u}_h + \mathcal{K}\varepsilon^{-1}G'(v_h)\big\|_{L^2(K)} \\
& + \frac{\mathcal{K}\varepsilon}{2}\, \|[\![\nabla v_h]\!]\|_{L^2(\partial K)} \left(\frac{h_K}{\lambda_{1,K}\lambda_{2,K}}\right)^{1/2} \\
& + \frac{\delta_{K,CR_{k-1}}}{\gamma_B}\, \|v_h\|_{L^2(K)} + \frac{h^2_K}{\lambda_{2,K}} \bigg(\big|F'(v_h)\big|_{W^{1,\infty}(K)}\, \|A\nabla\mathbf{u}_h \diamond \nabla\mathbf{u}_h\|_{L^2(K)} \\
& + \frac{|K|^{1/2}\mathcal{K}}{2\varepsilon}\, \big|G'(v_h)\big|_{W^{1,\infty}(K)} + \frac{|K|^{1/2}\delta_{K,CR_{k-1}}}{\gamma_B}\, |v_h|_{W^{1,\infty}(K)} \bigg),
\end{aligned}$$

with

$$[\![(A\nabla\mathbf{u}_h)_i]\!] = \begin{cases} [(A\nabla\mathbf{u}_h)_i\cdot\mathbf{n}]_e & e\in\mathcal{E}_h\cap\Omega \\ 2((A\nabla\mathbf{u}_h)_i\cdot\mathbf{n})\big|_e & e\in\mathcal{E}_h\cap\partial\Omega, \end{cases} \tag{16}$$

$$[\![\nabla v_h]\!] = \begin{cases} [\nabla v_h\cdot\mathbf{n}]_e & e\in\mathcal{E}_h\cap\Omega \\ 2(\nabla v_h\cdot\mathbf{n})\big|_e & e\in\mathcal{E}_h\cap\partial\Omega, \end{cases} \tag{17}$$

the generalized jumps, $[\cdot]_e$ *denoting the jump across the generic edge* e *of the skeleton* $\mathcal{E}_h$ *of* $\mathcal{T}_h$*, with* $\mathbf{n}$ *the unit normal vector to* e*.*

Proof. From equation (6), for any pair $(\boldsymbol{\phi},\psi)\in[H^1(\Omega)]^n\times H^1(\Omega)$ and for $\mathbf{u}=\mathbf{u}_h$, $v=v_h$, it holds

$$|J'(\mathbf{u}_h,v_h;\boldsymbol{\phi},\psi)|\le|a(v_h;\mathbf{u}_h,\boldsymbol{\phi})|+|b(\mathbf{u}_h;v_h,\psi)|.$$

Now, let us estimate the two terms on the right-hand side, separately.

Estimate for $a(v_h;\mathbf{u}_h,\boldsymbol{\phi})$ Since $a_h(v_h;\mathbf{u}_h,\boldsymbol{\phi}_h)=0$ for any $\boldsymbol{\phi}_h\in X_h$, $(\mathbf{u}_h,v_h)$ being a critical point of $a_h(\cdot;\cdot,\cdot)$, and thanks to the linearity of $a(\cdot;\cdot,\cdot)$ with respect to the third argument, we have

$$|a(v_h;\mathbf{u}_h,\boldsymbol{\phi})|\le|a(v_h;\mathbf{u}_h,\boldsymbol{\phi}-\boldsymbol{\phi}_h)|+|a(v_h;\mathbf{u}_h,\boldsymbol{\phi}_h)-a_h(v_h;\mathbf{u}_h,\boldsymbol{\phi}_h)|. \tag{18}$$

We tackle the two contributions on the right-hand side in (18) in turn.

Term $|a(v_h;\mathbf{u}_h,\boldsymbol{\phi}-\boldsymbol{\phi}_h)|$ Using (7), and Lemma 3.3, we obtain

$$\begin{aligned}
&|a(v_h;\mathbf{u}_h,\boldsymbol{\phi}-\boldsymbol{\phi}_h)|\\
&=\Big|\sum_{K\in\mathcal{T}_h}\Big[\int_K(F(v_h)+\eta)A\nabla\mathbf{u}_h\diamond\nabla(\boldsymbol{\phi}-\boldsymbol{\phi}_h)\,d\mathbf{x}\\
&+\frac{1}{\gamma_A}\int_K(\mathbf{u}_h-\mathbf{g}_D(t_k))\odot(\boldsymbol{\phi}-\boldsymbol{\phi}_h)\chi_{\Omega_D}\,d\mathbf{x}\Big]\Big|\\
&=\Big|\sum_{K\in\mathcal{T}_h}\Big[-\int_K\Big(F'(v_h)A\nabla\mathbf{u}_h\diamond\big((\boldsymbol{\phi}-\boldsymbol{\phi}_h)\times\nabla v_h\big)\\
&+F(v_h)\nabla\cdot(A\nabla\mathbf{u}_h)\odot(\boldsymbol{\phi}-\boldsymbol{\phi}_h)\Big)d\mathbf{x}\\
&+\int_{\partial K}(F(v_h)+\eta)A\nabla\mathbf{u}_h\diamond\big((\boldsymbol{\phi}-\boldsymbol{\phi}_h)\times\mathbf{n}\big)\,ds\\
&+\frac{1}{\gamma_A}\int_K\big(\mathbf{u}_h-\mathbf{g}_h(t_k)+\mathbf{g}_h(t_k)-\mathbf{g}_D(t_k)\big)\odot(\boldsymbol{\phi}-\boldsymbol{\phi}_h)\chi_{\Omega_D}\,d\mathbf{x}\Big]\Big|,
\end{aligned}$$

where χ_{Ω_D} denotes the characteristic function of Ω_D. By applying Lemma 3.3, the Cauchy-Schwarz inequality and definition (16), we have

$$
\begin{aligned}
&|a(v_h; \mathbf{u}_h, \boldsymbol{\phi} - \boldsymbol{\phi}_h)| \\
&\le \sum_{K\in\mathcal{T}_h} \sum_{i=1}^{n} \Big[\|F'(v_h)(A\nabla\mathbf{u}_h)_i \cdot \nabla v_h + F(v_h)\nabla\cdot(A\nabla\mathbf{u}_h)_i\|_{L^2(K)} \|\phi_i - \phi_{h,i}\|_{L^2(K)} \\
&+ \frac{1}{2} \|[\![(A\nabla\mathbf{u}_h)_i]\!]\|_{L^\infty(\partial K)} \|F(v_h) + \eta\|_{L^2(\partial K)} \|\phi_i - \phi_{h,i}\|_{L^2(\partial K)} \\
&+ \frac{\delta_{K,\Omega_D}}{\gamma_A} \Big(\|u_{h,i} - g_{h,i}(t_k)\|_{L^2(K)} + \|g_{h,i}(t_k) - g_i(t_k)\|_{L^2(K)} \Big) \|\phi_i - \phi_{h,i}\|_{L^2(K)} \Big],
\end{aligned}
$$

where $\delta_{K,\Omega_D} = 1$ if $K \subset \Omega_D$, and is equal to zero otherwise. Since this inequality holds for any $\boldsymbol{\phi}_h \in [X_h]^n$, we pick $\boldsymbol{\phi}_h$ such that $\phi_{h,i} = \mathcal{C}_h(\phi_i)$. Using Lemma 3.1 and definition (15), we obtain

$$
\begin{aligned}
&|a(v_h; \mathbf{u}_h, \boldsymbol{\phi} - \boldsymbol{\phi}_h)| \\
&\le C \sum_{K\in\mathcal{T}_h} \sum_{i=1}^{n} \Big[\|F'(v_h)(A\nabla\mathbf{u}_h)_i \cdot \nabla v_h + F(v_h)\nabla\cdot(A\nabla\mathbf{u}_h)_i\|_{L^2(K)} \\
&+ \frac{1}{2} \|[\![(A\nabla\mathbf{u}_h)_i]\!]\|_{L^\infty(\partial K)} \|F(v_h) + \eta\|_{L^2(\partial K)} \left(\frac{h_K}{\lambda_{1,K}\lambda_{2,K}} \right)^{1/2} \\
&+ \frac{\delta_{K,\Omega_D}}{\gamma_A} \Big(\|u_{h,i} - g_{h,i}(t_k)\|_{L^2(K)} + \|g_{h,i}(t_k) - g_i(t_k)\|_{L^2(K)} \Big) \Big] \omega_K(\phi_i).
\end{aligned}
$$

Notice that constant C may change value throughout this proof.

Term $|a(v_h; \mathbf{u}_h, \boldsymbol{\phi}_h) - a_h(v_h; \mathbf{u}_h, \boldsymbol{\phi}_h)|$ Recalling definitions (7) and (11), we have

$$
\begin{aligned}
|a(v_h; \mathbf{u}_h, \boldsymbol{\phi}_h) - a_h(v_h; \mathbf{u}_h, \boldsymbol{\phi}_h)| = \Big| &\int_\Omega (F(v_h) - P_h(F(v_h))) A\nabla\mathbf{u}_h \diamond \nabla\boldsymbol{\phi}_h \, d\mathbf{x} \\
&+ \frac{1}{\gamma_A} \int_{\Omega_D} (I - P_h)\left((\mathbf{u}_h - \mathbf{g}_h(t_k)) \odot \boldsymbol{\phi}_h \right) d\mathbf{x} \Big|,
\end{aligned}
$$

that componentwise, via Lemma 3.3, becomes

$$
\begin{aligned}
&|a(v_h; \mathbf{u}_h, \boldsymbol{\phi}_h) - a_h(v_h; \mathbf{u}_h, \boldsymbol{\phi}_h)| \\
&= \Big| \sum_{K\in\mathcal{T}_h} \sum_{i=1}^{n} \Big[\int_K \big((F(v_h) - P_h(F(v_h))) A\nabla\mathbf{u}_h \big)_i \cdot (\nabla\boldsymbol{\phi}_h)_i \, d\mathbf{x} \\
&+ \frac{1}{\gamma_A} \int_K (I - P_h)\left((u_{h,i} - g_{h,i}(t_k))\phi_{h,i} \right) \chi_{\Omega_D} \, d\mathbf{x} \Big] \Big|.
\end{aligned}
$$

Applying the Cauchy-Schwarz inequality, the interpolation estimate $\|v - P_h(v)\|_{L^2(K)} \le C h_K^2 |v|_{H^2(K)}$ and result $|w_h v_h|_{H^2(K)} \le 2|w_h|_{W^{1,\infty}(K)} \|\nabla v_h\|_{L^2(K)}$, for any $K \in \mathcal{T}_h$, we derive

$$
\begin{aligned}
&|a(v_h;\mathbf{u}_h,\boldsymbol{\phi}_h)-a_h(v_h;\mathbf{u}_h,\boldsymbol{\phi}_h)| \\
&\le \sum_{K\in\mathcal{T}_h}\sum_{i=1}^{n}\Bigg[\|F(v_h)-P_h(F(v_h))\|_{L^\infty(K)}\|(A\nabla\mathbf{u}_h)_i\|_{L^2(K)}\|\nabla\phi_{h,i}\|_{L^2(K)} \\
&+\frac{\delta_{K,\Omega_D}}{\gamma_A}|K|^{1/2}\|(I-P_h)((u_{h,i}-g_{h,i}(t_k))\phi_{h,i})\|_{L^2(K)}\Bigg] \\
&\le \sum_{K\in\mathcal{T}_h}\sum_{i=1}^{n}\Bigg[\|F(v_h)-P_h(F(v_h))\|_{L^\infty(K)}\|(A\nabla\mathbf{u}_h)_i\|_{L^2(K)}\|\nabla\phi_{h,i}\|_{L^2(K)} \\
&+\frac{C\delta_{K,\Omega_D}|K|^{1/2}h_K^2}{\gamma_A}|(u_{h,i}-g_{h,i}(t_k))\phi_{h,i}|_{H^2(K)}\Bigg] \\
&\le C\sum_{K\in\mathcal{T}_h}\sum_{i=1}^{n}\Bigg[\|F(v_h)-P_h(F(v_h))\|_{L^\infty(K)}\|(A\nabla\mathbf{u}_h)_i\|_{L^2(K)} \\
&+\frac{\delta_{K,\Omega_D}|K|^{1/2}h_K^2}{\gamma_A}|u_{h,i}-g_{h,i}(t_k)|_{W^{1,\infty}(K)}\Bigg]\Big(\|\nabla(\phi_{h,i}-\phi_i)\|_{L^2(K)}+\|\nabla\phi_i\|_{L^2(K)}\Big).
\end{aligned}
$$

In order to estimate $\|\nabla\phi_i\|_{L^2(K)}$, we use Lemma 3.2 with $\beta_i=\lambda_{i,K}^2$, $i=1,2$, and we apply Lemma 3.1 to estimate the norm $\|\nabla(\phi_{h,i}-\phi_i)\|_{L^2(K)}$, thus obtaining

$$
\begin{aligned}
&|a(v_h;\mathbf{u}_h,\boldsymbol{\phi}_h)-a_h(v_h;\mathbf{u}_h,\boldsymbol{\phi}_h)| \\
&\le C\sum_{K\in\mathcal{T}_h}\sum_{i=1}^{n}\Bigg[\|F(v_h)-P_h(F(v_h))\|_{L^\infty(K)}\|(A\nabla\mathbf{u}_h)_i\|_{L^2(K)} \\
&+\frac{\delta_{K,\Omega_D}|K|^{1/2}h_K^2}{\gamma_A}|u_{h,i}-g_{h,i}(t_k)|_{W^{1,\infty}(K)}\Bigg]\frac{1}{\lambda_{2,K}}\,\omega_K(\phi_i).
\end{aligned}
$$

Estimate for $a(v_h;\mathbf{u}_h,\boldsymbol{\phi})$ Combining the upper bounds for the two contributions on the right-hand side of (18), we have

$$
\begin{aligned}
|a(v_h;\mathbf{u}_h,\boldsymbol{\phi})| &\le C\sum_{K\in\mathcal{T}_h}\sum_{i=1}^{n}\Bigg[\|F'(v_h)(A\nabla\mathbf{u}_h)_i\cdot\nabla v_h+F(v_h)\nabla\cdot(A\nabla\mathbf{u}_h)_i\|_{L^2(K)} \\
&+\frac{1}{2}\,\|[\![(A\nabla\mathbf{u}_h)_i]\!]\|_{L^\infty(\partial K)}\,\|F(v_h)+\eta\|_{L^2(\partial K)}\left(\frac{h_K}{\lambda_{1,K}\lambda_{2,K}}\right)^{1/2} \\
&+\frac{\delta_{K,\Omega_D}}{\gamma_A}\Big(\|u_{h,i}-g_{h,i}(t_k)\|_{L^2(K)}+\|g_{h,i}(t_k)-g_i(t_k)\|_{L^2(K)}\Big) \\
&+\frac{1}{\lambda_{2,K}}\bigg(\|F(v_h)-P_h(F(v_h))\|_{L^\infty(K)}\|(A\nabla\mathbf{u}_h)_i\|_{L^2(K)} \\
&+\frac{\delta_{K,\Omega_D}|K|^{1/2}h_K^2}{\gamma_A}|u_{h,i}-g_{h,i}(t_k)|_{W^{1,\infty}(K)}\bigg)\Bigg]\omega_K(\phi_i) \\
&= C\sum_{K\in\mathcal{T}_h}\sum_{i=1}^{n}\rho_{i,K}^{A}(v_h,\mathbf{u}_h)\omega_K(\phi_i).
\end{aligned}
$$

Estimate for $b(\mathbf{u}_h; v_h, \psi)$ Since $b_h(\mathbf{u}_h; v_h, \psi_h) = 0$, for any $\psi_h \in X_h$, and thanks to the the linearity of $b(\cdot; \cdot, \cdot)$ with respect to the third argument, we have

$$|b(\mathbf{u}_h; v_h, \psi)| \leq |b(\mathbf{u}_h; v_h, \psi - \psi_h)| + |b(\mathbf{u}_h; v_h, \psi_h) - b_h(\mathbf{u}_h; v_h, \psi_h)|. \tag{19}$$

Let us estimate the two terms on the right-hand side, separately.

Term $|b(\mathbf{u}_h; v_h, \psi - \psi_h)|$ By exploiting definition (8), we have

$$\begin{aligned} |b(\mathbf{u}_h; v_h, \psi - \psi_h)| = \bigg| \frac{1}{2} \int_\Omega F'(v_h)(\psi - \psi_h) A \nabla \mathbf{u}_h \diamond \nabla \mathbf{u}_h \, d\mathbf{x} \\ + \frac{\mathcal{K}}{2} \int_\Omega \left(\varepsilon^{-1} G'(v_h)(\psi - \psi_h) + 2\varepsilon \nabla v_h \cdot \nabla(\psi - \psi_h) \right) d\mathbf{x} + \frac{1}{\gamma_B} \int_{CR_{k-1}} v_h(\psi - \psi_h) \, d\mathbf{x} \bigg|. \end{aligned}$$

Integrating elementwise by parts the third term, using the Cauchy-Schwarz inequality, definition (17) and since $\Delta v_h \big|_K = 0$ as $v_h \in X_h$, it follows

$$\begin{aligned} &|b(\mathbf{u}_h; v_h, \psi - \psi_h)| \\ &\leq \sum_{K \in \mathcal{T}_h} \left[\frac{1}{2} \left\| F'(v_h) A \nabla \mathbf{u}_h \diamond \nabla \mathbf{u}_h + \mathcal{K} \varepsilon^{-1} G'(v_h) \right\|_{L^2(K)} \|\psi - \psi_h\|_{L^2(K)} \right. \\ &\left. + \frac{\mathcal{K}\varepsilon}{2} \|[\![\nabla v_h]\!]\|_{L^2(\partial K)} \|\psi - \psi_h\|_{L^2(\partial K)} + \frac{\delta_{K, CR_{k-1}}}{\gamma_B} \|v_h\|_{L^2(K)} \|\psi - \psi_h\|_{L^2(K)} \right], \end{aligned}$$

where $\delta_{K, CR_{k-1}} = 1$ if $K \subset CR_{k-1}$ and vanishes otherwise. We pick $\psi_h = \mathcal{C}_h(\psi)$ and we apply Lemma 3.1, thus obtaining

$$\begin{aligned} &|b(\mathbf{u}_h; v_h, \psi - \psi_h)| \\ &\leq C \sum_{K \in \mathcal{T}_h} \left[\frac{1}{2} \left\| F'(v_h) A \nabla \mathbf{u}_h \diamond \nabla \mathbf{u}_h + \mathcal{K} \varepsilon^{-1} G'(v_h) \right\|_{L^2(K)} \right. \\ &\left. + \frac{\mathcal{K}\varepsilon}{2} \|[\![\nabla v_h]\!]\|_{L^2(\partial K)} \left(\frac{h_K}{\lambda_{1,K} \lambda_{2,K}} \right)^{1/2} + \frac{\delta_{K, CR_{k-1}}}{\gamma_B} \|v_h\|_{L^2(K)} \right] \omega_K(\psi). \end{aligned}$$

Term $|b(\mathbf{u}_h; v_h, \psi_h) - b_h(\mathbf{u}_h; v_h, \psi_h)|$ Using definitions (8) and (12), we have

$$\begin{aligned} |b(\mathbf{u}_h; v_h, \psi_h) - b_h(\mathbf{u}_h; v_h, \psi_h)| = \bigg| \frac{1}{2} \int_\Omega (I - P_h)(F'(v_h)\psi_h) A \nabla \mathbf{u}_h \diamond \nabla \mathbf{u}_h \, d\mathbf{x} \\ + \frac{\mathcal{K}}{2} \int_\Omega \varepsilon^{-1} (I - P_h)(G'(v_h)\psi_h) \, d\mathbf{x} + \frac{1}{\gamma_B} \int_{CR_{k-1}} (I - P_h)(v_h \psi_h) \, d\mathbf{x} \bigg|. \end{aligned}$$

By mimicking the same procedure adopted to bound $|a(v_h;\mathbf{u}_h,\boldsymbol{\phi}_h)-a_h(v_h;\mathbf{u}_h,\boldsymbol{\phi}_h)|$, we derive

$$
\begin{aligned}
&|b(\mathbf{u}_h;v_h,\psi_h)-b_h(\mathbf{u}_h;v_h,\psi_h)| \\
&\le \sum_{K\in\mathcal{T}_h}\Bigg[\,\|(I-P_h)(F'(v_h)\psi_h)\|_{L^2(K)}\,\|A\nabla\mathbf{u}_h\diamond\nabla\mathbf{u}_h\|_{L^2(K)} \\
&+\frac{|K|^{1/2}\mathcal{K}}{2\varepsilon}\,\|(I-P_h)(G'(v_h)\psi_h)\|_{L^2(K)}+\frac{|K|^{1/2}\delta_{K,CR_{k-1}}}{\gamma_B}\,\|(I-P_h)(v_h\psi_h)\|_{L^2(K)}\Bigg] \\
&\le C\sum_{K\in\mathcal{T}_h}h_K^2\Bigg[\,|F'(v_h)|_{W^{1,\infty}(K)}\,\|A\nabla\mathbf{u}_h\diamond\nabla\mathbf{u}_h\|_{L^2(K)}+\frac{|K|^{1/2}\mathcal{K}}{2\varepsilon}\,|G'(v_h)|_{W^{1,\infty}(K)} \\
&+\frac{|K|^{1/2}\delta_{K,CR_{k-1}}}{\gamma_B}\,|v_h|_{W^{1,\infty}(K)}\Bigg]\Big(\|\nabla\psi_h-\nabla\psi\|_{L^2(K)}+\|\nabla\psi\|_{L^2(K)}\Big) \\
&\le C\sum_{K\in\mathcal{T}_h}\frac{h_K^2}{\lambda_{2,K}}\Bigg[\,|F'(v_h)|_{W^{1,\infty}(K)}\,\|A\nabla\mathbf{u}_h\diamond\nabla\mathbf{u}_h\|_{L^2(K)} \\
&+\frac{|K|^{1/2}\mathcal{K}}{2\varepsilon}\,|G'(v_h)|_{W^{1,\infty}(K)}+\frac{|K|^{1/2}\delta_{K,CR_{k-1}}}{\gamma_B}\,|v_h|_{W^{1,\infty}(K)}\Bigg]\omega_K(\psi).
\end{aligned}
$$

Estimate for $b(\mathbf{u}_h;v_h,\psi)$ The separate upper bounds for the two terms on the right-hand side of (19) yield the estimate

$$
\begin{aligned}
|b(\mathbf{u}_h;v_h,\psi)| \le C\sum_{K\in\mathcal{T}_h}&\Bigg[\frac{1}{2}\left\|F'(v_h)A\nabla\mathbf{u}_h\diamond\nabla\mathbf{u}_h+\mathcal{K}\varepsilon^{-1}G'(v_h)\right\|_{L^2(K)} \\
&+\frac{\mathcal{K}\varepsilon}{2}\,\|[\![\nabla v_h]\!]\|_{L^2(\partial K)}\left(\frac{h_K}{\lambda_{1,K}\lambda_{2,K}}\right)^{1/2}+\frac{\delta_{K,CR_{k-1}}}{\gamma_B}\,\|v_h\|_{L^2(K)} \\
&+\frac{h_K^2}{\lambda_{2,K}}\Bigg(\,|F'(v_h)|_{W^{1,\infty}(K)}\,\|A\nabla\mathbf{u}_h\diamond\nabla\mathbf{u}_h\|_{L^2(K)} \\
+\frac{|K|^{1/2}\mathcal{K}}{2\varepsilon}\,|G'(v_h)|_{W^{1,\infty}(K)}&+\frac{|K|^{1/2}\delta_{K,CR_{k-1}}}{\gamma_B}\,|v_h|_{W^{1,\infty}(K)}\Bigg)\Bigg]\omega_K(\psi) \\
=C\sum_{K\in\mathcal{T}_h}\rho_K^B(\mathbf{u}_h,v_h)\omega_K(\psi).&
\end{aligned}
$$

□

According to Corollary 3.4 in [5], we choose $\phi_i=u_i-u_{h,i}$ and $\psi=v-v_h$ in (14). This allows us to control the error $J(\mathbf{u},v)-J(\mathbf{u}_h,v_h)$, which coincides with $J'(\mathbf{u}_h,v_h;\boldsymbol{\phi},\psi)$ up to a third-order term in $\mathbf{u}-\mathbf{u}_h$ and $v-v_h$. Thus, the resulting anisotropic a posteriori error estimator is represented by

$$
\eta=\sum_{K\in\mathcal{T}_h}\eta_K(\mathbf{u}_h,v_h),
$$

where the local error estimator is

$$
\eta_K(\mathbf{u}_h,v_h)=\sum_{i=1}^{n}\rho_{i,K}^A(v_h,\mathbf{u}_h)\omega_K^R(u_i-u_{h,i})+\rho_K^B(\mathbf{u}_h,v_h)\omega_K^R(v-v_h),
$$

with

$$\omega_K^R(z - z_h) = \left[\sum_{j=1}^{2} \lambda_{j,K}^2 \left(\mathbf{r}_{j,K}^T G_{\Delta_K}^R (z - z_h) \mathbf{r}_{j,K} \right) \right]^{1/2} \quad \text{with } z = u_i, v.$$

In particular, $G_{\Delta_K}^R(z - z_h)$ is the matrix with lm-entry

$$\left[G_{\Delta_K}^R (z - z_h) \right]_{lm} = \sum_{T \in \Delta_K} \int_T \left(R_l(z_h) - \frac{\partial z_h}{\partial x_l} \right) \left(R_m(z_h) - \frac{\partial z_h}{\partial x_m} \right) d\mathbf{x} \quad l, m = 1, 2,$$

where $R_l(z_h)$ is the recovered partial derivative of z_h with respect to x_l, for $l = 1, 2$ [26, 29, 27, 28].

4 The adaptive numerical algorithm

In this section, we focus on the numerical method for solving the minimization problem (10), based on an adaptive procedure. At each time level, the minimization of the functional is combined with a mesh adaptation strategy.

4.1 Metric-based mesh adaptation

We adopt the approach in [15, 22, 14, 23]. A metric is a symmetric positive definite tensor field $\mathcal{M} : \Omega \to \mathbb{R}^{2\times 2}$, which, for $\mathbf{x} \in \Omega$, provides the size of the optimal mesh along all the directions around $\mathbf{x}$. In practice, we approximate $\mathcal{M}$ via a piecewise constant metric on a given mesh $\mathcal{T}_h$ such that $\mathcal{M}|_K = R_K^T \Lambda_K^{-2} R_K$, for any $K \in \mathcal{T}_h$, where R_K and Λ_K are defined as in Section 3.1. Notice that whereas in Section 3.1 it is understood that $\mathcal{T}_h$ is given, here $\mathcal{T}_h$ is the actual unknown of the adaptive procedure. Estimator η will help us in providing the metric associated with the unknown mesh. Once the metric is defined, the corresponding mesh is built using the mesh generator BAMG of `FreeFem++` [20].

The unknown mesh is built by minimizing the number of elements, while guaranteeing a given accuracy `TOL` on the global error estimator η. In particular, we resort to an iterative procedure, which, at each step, first solves a constrained minimization problem for the local metric on each element of the current mesh, and then updates the mesh via BAMG with the derived metric as an input. We provide the result about the constrained minimization problem, by referring to [23] for all the details.

Proposition 4.1 *The solution to the local constrained minimization problem identifies the metric whose entries are*

$$\mathbf{r}_{1,K} = \boldsymbol{\gamma}_{2,K}, \quad \mathbf{r}_{2,K} \cdot \mathbf{r}_{1,K} = 0,$$

$$\lambda_{1,K} = \left(\frac{1}{|\hat{K}|\sqrt{2}} \left(\frac{g_{1,K}}{g_{2,K}^2} \right)^{1/2} \frac{\mathtt{TOL}}{\#\mathcal{T}_h} \right)^{1/3}, \quad \lambda_{2,K} = \left(\frac{1}{|\hat{K}|\sqrt{2}} \left(\frac{g_{2,K}}{g_{1,K}^2} \right)^{1/2} \frac{\mathtt{TOL}}{\#\mathcal{T}_h} \right)^{1/3},$$

where $\{\boldsymbol{\gamma}_{i,K}, g_{i,K}\}$, $i = 1, 2$, *are the eigenvector-eigenvalue pairs of the weighted-residual matrix*

$$\Gamma_K = \sum_{i=1}^{n} [\bar{\rho}^A_{i,K}(v_h, \mathbf{u}_h)]^2 \bar{G}^R_{\Delta_K}(u_i - u_{h,i}) + [\bar{\rho}^B_K(\mathbf{u}_h, v_h)]^2 \bar{G}^R_{\Delta_K}(v - v_h),$$

with

$$\bar{\rho}^A_{i,K}(v_h, \mathbf{u}_h) = \frac{\rho^A_{i,K}(v_h, \mathbf{u}_h)}{(|\hat{K}|\lambda_{1,K}\lambda_{2,K})^{1/2}}, \qquad \bar{\rho}^B_K(\mathbf{u}_h, v_h) = \frac{\rho^B_K(\mathbf{u}_h, v_h)}{(|\hat{K}|\lambda_{1,K}\lambda_{2,K})^{1/2}}$$

and $\bar{G}^R_{\Delta_K}(\cdot) = G^R_{\Delta_K}(\cdot)/(|\hat{K}|\lambda_{1,K}\lambda_{2,K})$.

4.2 The optimize-while-adapt numerical procedure

The full adaptive algorithm is obtained by combining the mesh adaptive procedure with the solution to the optimization problem (10). For this purpose, we generalize the algorithm proposed in [4] by considering general expressions for functions F and G. The algorithm is implemented in `FreeFem++`.

Given an initial mesh $\mathcal{T}_h^0$, the adopted procedure is itemized in Algorithm 1.

Algorithm 1: Optimize-while-Adapt algorithm

for $k = 0, \cdots, N$ **do**
- `set l=0; errmesh=1; err=1;`
- `if` $k = 0$, `set` v_h^0`=1; else` $v_h^0 = v_h(t_{k-1})$;
- **while** `((errmesh` $>$ `MESHTOL` $|$ `err` $>$ `VTOL)` $\&$ `l` $<$ `nADAPT)` **do**
  - `set i=0;`
  - **while** `(err` $>$ `VTOL` $\&$ `i` $<$ `nMIN)` **do**
    - $\mathbf{u}_h^{\mathtt{i}}$=argmin$_{\mathbf{z}_h \in [X_h^{(\mathtt{l})}]^n}$ $J_h(\mathbf{z}_h, v_h^{\mathtt{i}})$;
    - $v_h^{\mathtt{i+1}}$=argmin$_{z_h \in X_h^{(\mathtt{l})}}$ $J_h(\mathbf{u}_h^{\mathtt{i}}, z_h)$;
    - `err`$=\|v_h^{\mathtt{i+1}} - v_h^{\mathtt{i}}\|_{L^\infty(\Omega)}$;
    - `i=i+1;`
  - `compute metric` $\mathcal{M}^{(l+1)}$ `based on` $\mathbf{u}_h^{\mathtt{i}-1}$, $v_h^{\mathtt{i}}$ `and TOL;`
  - `build the adapted mesh` $\mathcal{T}_h^{(\mathtt{l+1})}$, `associated with` $\mathcal{M}^{(\mathtt{l+1})}$;
  - `errmesh`$=|\#\mathcal{T}_h^{(\mathtt{l+1})} - \#\mathcal{T}_h^{(\mathtt{l})}|/\#\mathcal{T}_h^{(\mathtt{l})}$;
  - `set` $v_h^0 = \Pi_{\mathtt{l}\to\mathtt{l+1}}(v_h^{\mathtt{i}})$;
  - `l=l+1;`
- `set` $\mathbf{u}_h(t_k) = \Pi_{\mathtt{l-1}\to\mathtt{l}}(\mathbf{u}_h^{\mathtt{i}-1})$; $v_h(t_k) = \Pi_{\mathtt{l-1}\to\mathtt{l}}(v_h^{\mathtt{i}})$; $\mathcal{T}_h^k = \mathcal{T}_h^{(\mathtt{l})}$;
- `set` $\mathcal{T}_h^{(0)} = \mathcal{T}_h^{(k)}$; $k = k + 1$;

The algorithm alternates the optimization through a fixed-point scheme with a maximum number `nMIN` of iterations, to mesh adaptation, until the convergence is reached. In particular, mesh adaptation is driven by tolerance `MESHTOL` which monitors mesh stagnation; the minimization of J_h is controlled by the increment on the phase field v_h to within a tolerance `VTOL`. Moreover, a maximum number, `nADAPT`, of global iterations is fixed to ensure termination of the whole procedure. Operator $\Pi_{\mathtt{n}\to\mathtt{n+1}}$ is used to interpolate the finite element functions defined on $\mathcal{T}_h^{(\mathtt{n})}$ onto the new mesh $\mathcal{T}_h^{(\mathtt{n+1})}$.

According to the form of F and G, the minimization of the functional J_h is performed differently. In particular, if we are dealing with the classical Ambrosio-Tortorelli functional ($F(v) = v^2$, $G(v) = (1-v)^2/4$), J_h is strictly convex with respect to each variable. In such a case, the Euler-Lagrange equations, associated with the minimization of the functional, correspond to second-order elliptic problems which are then approximated by a finite element method. On the contrary, when F and G are linear functions, J_h is strictly convex only with respect to $\mathbf{u}_h$. Therefore, we compute the minimum of J_h with respect to v_h via the `FreeFem++` function IPOPT [25]. This function implements an interior point optimization algorithm, to approximate a local solution of a constrained minimization problem. In this case, we enforce the irreversibility condition by requiring

$$v_h^{(\mathtt{i+1})} \leq \begin{cases} v_h(t_{k-1}) & \text{if } v_h(t_{k-1}) < \mathtt{CRTOL} \\ 1 & \text{elsewhere,} \end{cases}$$

by neglecting the corresponding penalty term in J_h.

5 Numerical assessment

We validate the performance of the proposed adaptive procedure by comparing the corresponding results with the literature.

We particularize the gAT functional for two choices of the elasticity law, i.e., the plane-strain and anti-plane strain configurations. In the first case, $\mathbf{u} : \Omega \to \mathbb{R}^2$ is a vector field and $A\nabla\mathbf{u}\diamond\nabla\mathbf{u} = \boldsymbol{\sigma}(\boldsymbol{u}) : \boldsymbol{\varepsilon}(\boldsymbol{u})$, where $\boldsymbol{\sigma} = 2\mu\boldsymbol{\varepsilon} + \lambda \mathrm{tr}(\boldsymbol{\varepsilon}) I$ is the Cauchy stress tensor, λ and μ are the Lamé constants and $\boldsymbol{\varepsilon} = (\nabla\boldsymbol{u} + (\nabla\boldsymbol{u})^T)/2$ is the strain tensor. The relations between the Lamé constants, the Young modulus E and the Poisson ratio ν for homogeneous isotropic elastic media are

$$\lambda = \frac{E\nu}{(1+\nu)(1-2\nu)}, \quad \mu = \frac{E}{2(1+\nu)}.$$

In the second case, $\mathbf{u}$ reduces to the scalar field $u : \Omega \to \mathbb{R}$ and $A\nabla\mathbf{u}\diamond\nabla\mathbf{u} = |\nabla u|^2$.

Three test cases are presented. In the first one, we check the consistency of the adaptive method with [4], in the case of plane-strain elasticity, with the classical Ambrosio-Tortorelli functional. The second test case investigates different choices for F and G in anti-plane configurations, and deal with the gAT functional, while the last test case considers quadratic functions F and G, under plane-strain conditions on a new benchmark.

5.1 Test case I

We consider the crack branching test case in [6], where $\Omega = (-1.5, 1.5)^2$ is characterized by a horizontal initial slit of length 1.5 and thickness $2 \cdot 10^{-}5$ (see Figure 2), under plane-strain elasticity, with $E = 45$ and $\nu = 0.18$ (i.e., $\lambda = 10.73$ and $\mu = 19.07$). An increasing in time displacement, with constant orientation θ with respect to the x_1-direction, is applied on top and bottom of the domain in opposite directions, as shown in Figure 2.

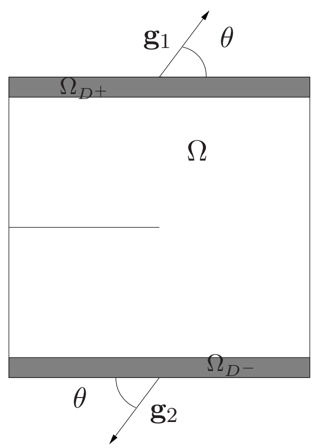

Figure 2: Test Case I: geometric configuration.

In particular, Ω_D consists of two subdomains, $\Omega_{D^-} = (-1.5, 1.5) \times (-1.5, -1.3)$ and $\Omega_{D^+} = (-1.5, 1.5) \times (1.3, 1.5)$, while $\mathbf{g}_D(t)$ is defined as

$$\mathbf{g}_D(t) = \begin{cases} \mathbf{g}_1(t) = (t\cos(\theta), t\sin(\theta)) & \text{on } \Omega_{D^+} \\ \mathbf{g}_2(t) = (-t\cos(\theta), -t\sin(\theta)) & \text{on } \Omega_{D^-}, \end{cases}$$

for $\theta = \{\pi/2, \pi/4, \pi/6, \pi/20, \pi/60, 0\}$. The final time is $T = 0.23$ and the number of time steps is $N = 23$. To compare with [4], we adopt the classical Ambrosio-Tortorelli functional with $\varepsilon = 10^{-2}$, $\mathcal{K} = 1$, $\eta = 10^{-5}$, $\gamma_A = \gamma_B = 10^{-5}$, $\texttt{CRTOL} = 3 \cdot 10^{-4}$.

The parameters involved in Algorithm 1 are set to $\texttt{VTOL} = 10^{-4}$, $\texttt{MESHTOL} = 10^{-2}$, $\texttt{TOL} = 10^{-3}$, $\texttt{nADAPT} = 50$, $\texttt{nMIN} = 7$.

In Figure 3, we show the phase-field v_h for different choices of the angle θ. The results are in agreement with the ones in Figure 6 of [4] from a qualitative viewpoint. In particular, we observe that the branching angle depends, as expected, on θ.

In Figure 4, we provide the adapted meshes for $\theta = \pi/2$ (top) and $\theta = 0$ (bottom). In both cases, the anisotropic features of the mesh are evident along the crack whereas the mesh is essentially isotropic on the crack tip and, as expect, far off the crack. In particular, the maximum aspect ratio s_K is on the order of 10^2 for all the choices of θ, being largest for $\theta = \pi/60$ ($\max_K s_K = 713$) and smallest for $\theta = \pi/6$ ($\max_K s_K = 352$).

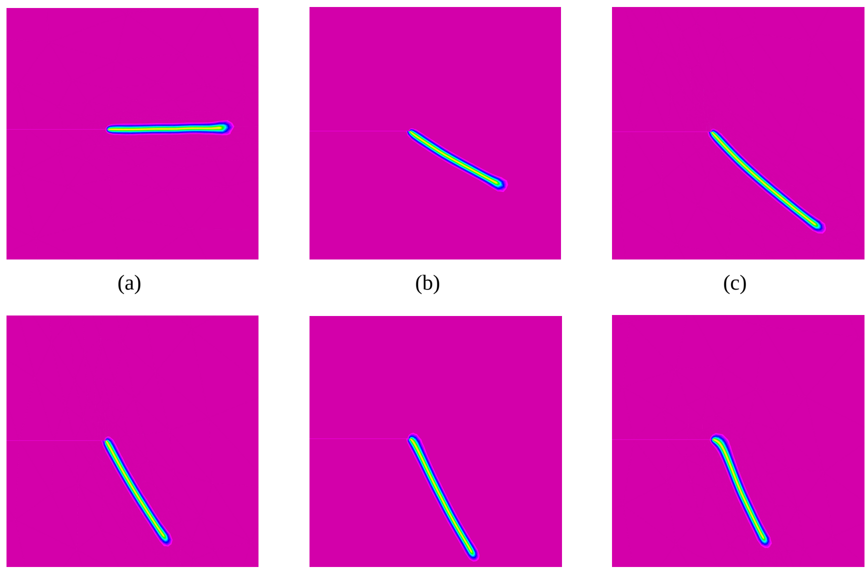

Figure 3: Test case I: detail of the v_h-field around the crack for $\theta = \{\pi/2, \pi/4, \pi/6, \pi/20, \pi/60, 0\}$ (left-right, top-bottom).

In Figure 5, we plot the branching angle as a function of the orientation θ. We consider the angle with respect to the x_1-axis, computed by picking the angle at which the distribution of the unit vectors, $\mathbf{r}_{1,K}$, gathered in bins of 20 angles each, over the rectangle $[0, 0.08] \times [-0.08, 0]$ is a maximum. We observe a good agreement with the results in [4]. In particular, the reliability of Algorithm 1 is guaranteed for angles $\theta \gtrsim 3°$ in contrast to [6] where the lower bound for θ is about $7°$.

5.2 Test case II

We compare the results provided by the proposed adaptive procedure with [8] by considering the gAT functional for different choices of F, G. Moreover, we perform a sensitivity analysis to ε and `TOL`.

The domain is the plate $\Omega = (0, 2) \times (0, 2.1)$ exhibiting a circular hole of radius 0.7 in the bottom-left corner (see Figure 6) and an initial vertical slit of length 0.6 and thickness $2 \cdot 10^{-5}$. An anti-plane strain condition is applied to the plate. In particular, a growing in time displacement $g_D(t)$ is applied on the two upper parts of the domain, orthogonally to the plane and in opposite directions, with

$$g_D(t) = \begin{cases} t & \text{on } \Omega_{D^+} \\ -t & \text{on } \Omega_{D^-}, \end{cases}$$

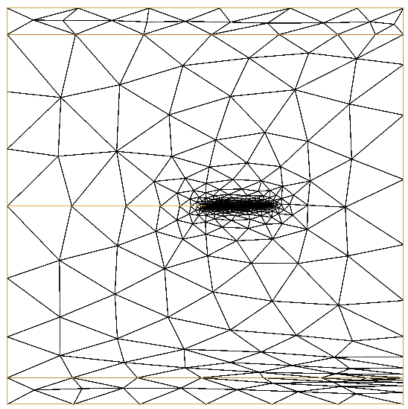

(a) $\theta = \pi/2$ - 3591 triangles

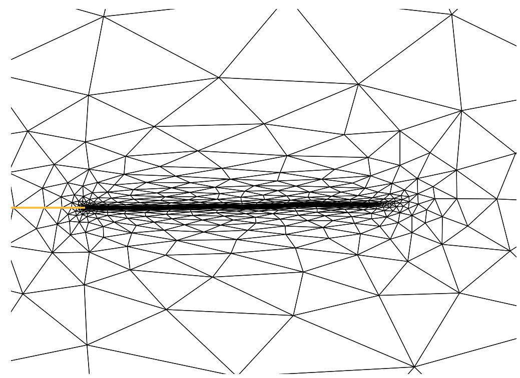

(b) $\theta = \pi/2$ - zoom

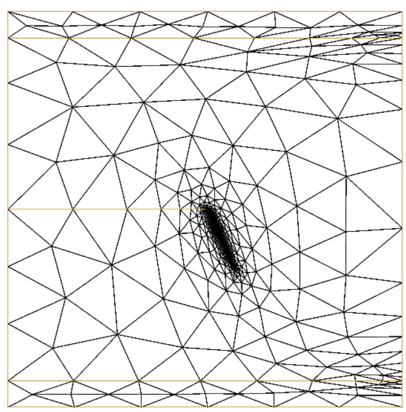

(c) $\theta = 0$ - 4775 triangles

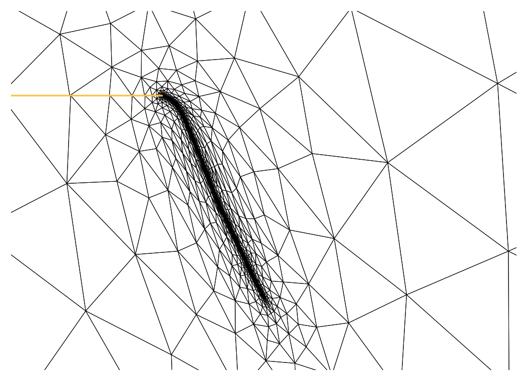

(d) $\theta = 0$ - zoom

Figure 4: Test case I: adapted grids for $\theta = \pi/2$ (top) and $\theta = 0$ (bottom) and corresponding details on the right.

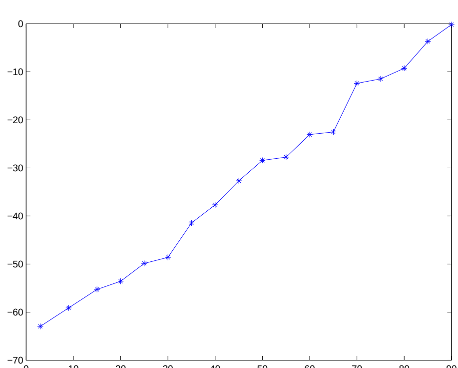

Figure 5: Test case I: branching angle as a function of the orientation of the applied displacement.

where $\Omega_{D^-} = (0,1) \times (2, 2.1)$ and $\Omega_{D^+} = (1,2) \times (2, 2.1)$. Moreover, we set $\mathcal{K} = 1$, $\eta = \varepsilon^2$, $\gamma_A = \gamma_B = 10^{-4}$, CRTOL $= 10^{-3}$. The final time is $T = 1.5$ and the number of time steps is $N = 150$.

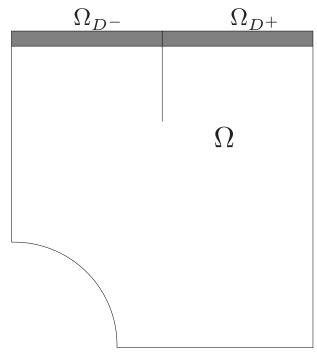

Figure 6: Test Case II: geometric configuration.

Following [8], the different choices of F and G are identified by the following notation:
quadratic: J_{22}: $F(v) = v^2$, $G(v) = (1-v)^2/4$;
linear: J_{11}: $F(v) = v$, $G(v) = 9(1-v)/64$;
mixed: J_{21}: $F(v) = v^2$, $G(v) = 9(1-v)/64$.

In Algorithm 1, we set the input parameters as VTOL $= 10^{-3}$, MESHTOL $= 10^{-2}$, TOL $= 10^{-2}$, nADAPT $= 10$, nMIN $= 20$.

Sensitivity with respect to ε

In this first check, we adopt the linear choice J_{11}. In Figure 7, we compare the phase-field v_h and the energy distribution, for different choices of ε. In particular, we distinguish between elastic and fracture energy, represented by the first and the second integral in (1), respectively. The total energy is clearly the sum of these two contributions.

We observe that for $\varepsilon \to 0$, a higher energy is demanded to initiate the crack propagation. Consistently with [3], the crack thickness reduces as ε decreases. The path of the crack is also influenced by ε, in particular with respect to the breaking point on the circular profile.

Sensitivity with respect to TOL

We refer to J_{11} also for this check, by choosing the smallest value for ε in view of the previous check, $\varepsilon = 0.02$. Figure 8 collects the corresponding results. We notice that if TOL is large (e.g., TOL $= 3 \cdot 10^{-2}$), the predicted crack path fails to detect the expected behavior. Nevertheless, if TOL is small, the number of mesh element increases. For instance, when TOL $= 7 \cdot 10^{-3}$ the number of mesh elements at $t = T$ is 3020, while for TOL $= 10^{-2}$, 2634 elements suffice.

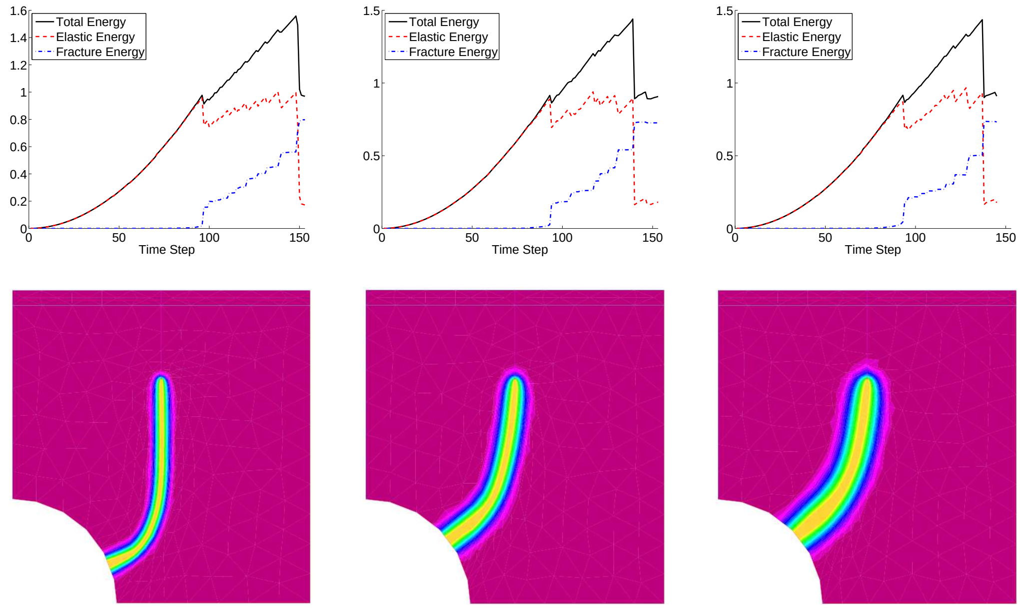

(a) $\varepsilon = 0.02$ (b) $\varepsilon = 0.03$ (c) $\varepsilon = 0.04$

Figure 7: Test Case II : energy distribution (top) and v_h-field (bottom) for different choices of ε and for the linear case J_{11}.

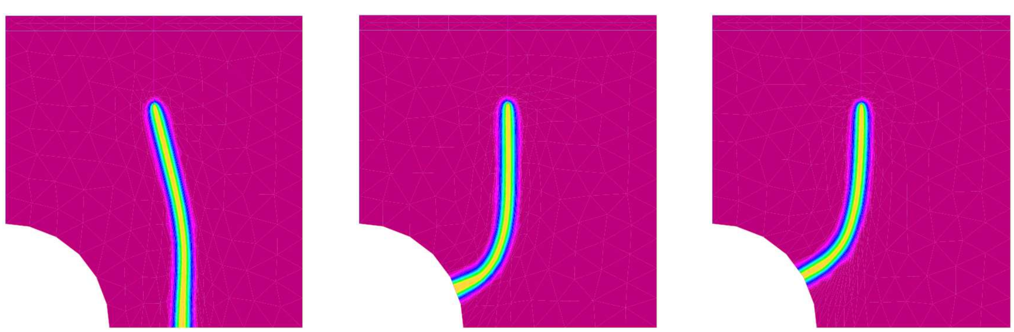

(a) $\texttt{TOL}= 3 \cdot 10^{-2}$ (b) $\texttt{TOL}= 10^{-2}$ (c) $\texttt{TOL}= 7 \cdot 10^{-3}$

Figure 8: Test Case II : phase-field v_h for different choices of TOL and for the linear case J_{11}.

The tuning of the parameters may obviously benefit of a reduced number of elements.

Anisotropic vs isotropic mesh adaptation

We finally compare the performance of Algorithm 1 with the results in [8], Figure 3. In particular, we focus on both the qualitative behavior of the crack path and on the cardinality of the final adapted grid.

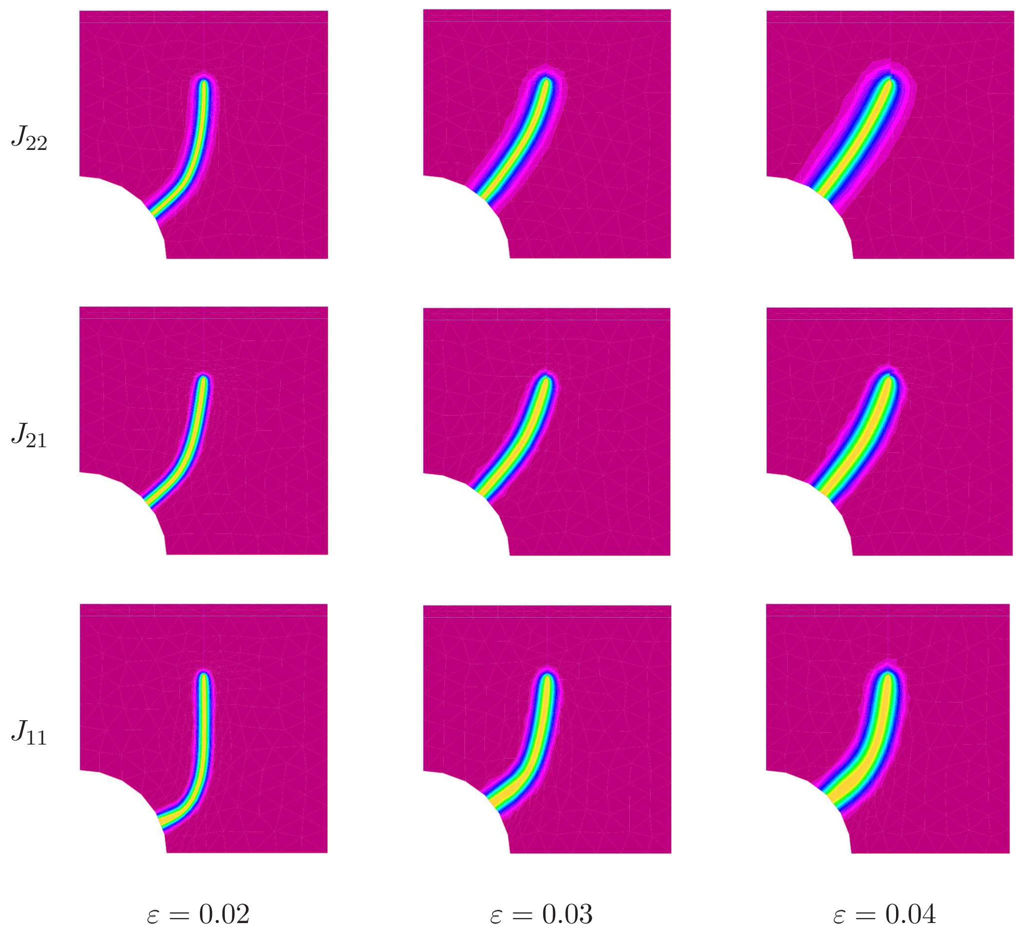

Figure 9: Test Case II : v_h-field for different choices of F and G (by rows) and ε (by columns).

The crack path shown in Figure 9 is in agreement with the results in [8] by exhibiting the same trend according to the linear or quadratic nature of F and G. Apparently, the case J_{11} is more robust in preserving the expected shape of the crack path. Moreover, we notice that the anisotropic adapted meshes sharply capture the crack path, with a very reduced number of triangles. For instance, the number of mesh elements in [8] is about 100000 for J_{22} and 500000 for J_{11}.

The anisotropic meshes cut off drastically this number, which is about two orders of magnitude less (see Figure 10 for the actual cardinalities). Moreover, we notice that the number of elements decreases for increasing values of ε. Concerning the anisotropic features of the elements, the maximum aspect ratio of the meshes in Figure 10 varies between 64 and 630, as reported in Table 1.

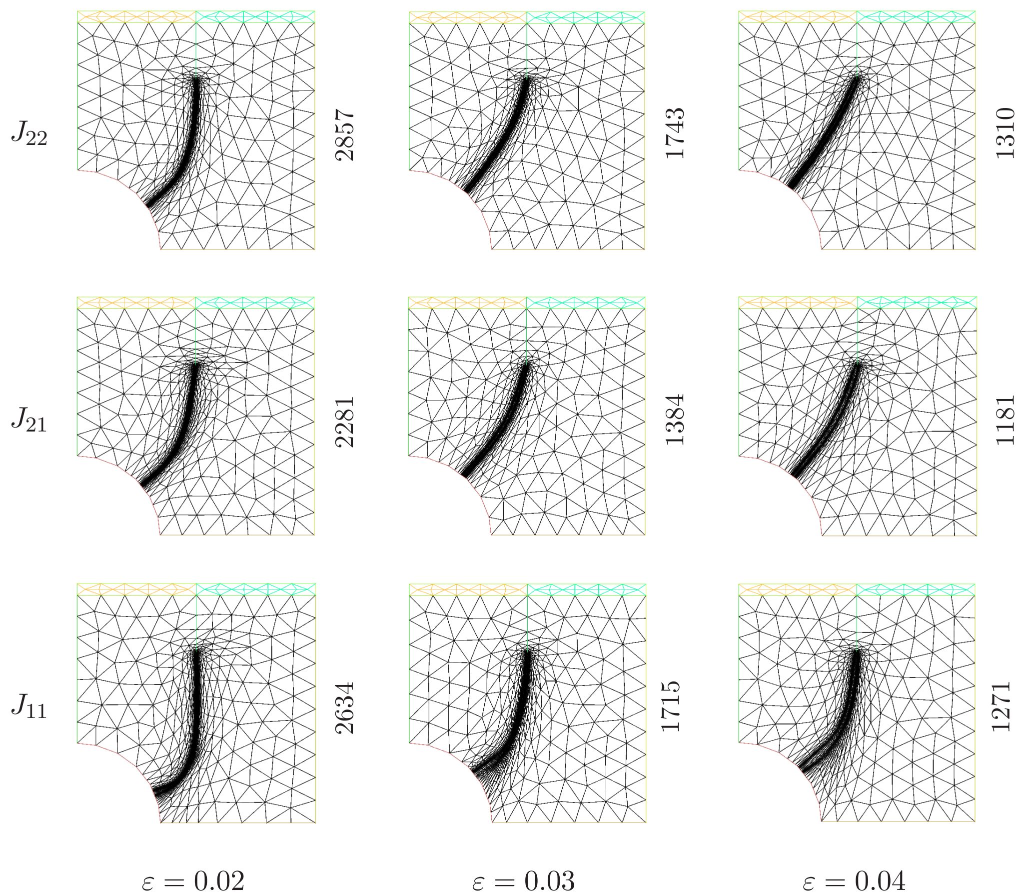

Figure 10: Test Case II : anisotropic adapted meshes for different choices of F and G (by rows) and ε (by columns). The cardinality is provided next to the meshes.

5.3 Test Case III

We focus on the benchmark problem in [24]. We consider the rectangular plate $\Omega = (0, 8) \times (0, 2)$, under plane-strain elasticity, with a triangular slit on the bottom edge (see Figure 11). An increasing in time vertical displacement is applied on $\Gamma_{D,1} = (3.9, 4.1) \times \{2\}$, while a homogeneous Dirichlet boundary condition is applied on $\Gamma_{D,2} = (0, 0.1) \times \{0\}$ and a vanishing vertical displacement is enforced on $\Gamma_{D,3} = (7.9, 8) \times \{0\}$. The final time is $T = 3.5$ and the number

	$\varepsilon = 0.02$	$\varepsilon = 0.03$	$\varepsilon = 0.04$
J_{11}	$6.3 \cdot 10^2$	$1.0 \cdot 10^2$	$2.0 \cdot 10^2$
J_{21}	$1.6 \cdot 10^2$	$1.8 \cdot 10^2$	$6.6 \cdot 10^1$
J_{22}	$7.9 \cdot 10^1$	$6.4 \cdot 10^1$	$1.2 \cdot 10^2$

Table 1: Test Case II : maximum aspect ratio for different choices of F and G (by rows) and ε (by columns).

of time steps is $N = 3500$. The applied displacement consists of increments of 10^{-4} for the first 360 steps, and of 10^{-5} successively.

To be consistent with [24], we choose $F(v) = v^2$ and $G(v) = (1-v)^2$ in the gAT functional, for $\mathcal{K} = 0.5$ $\eta = 10^{-6}$, $\gamma_A = \gamma_B = 10^{-5}$, $\texttt{CRTOL} = 10^{-6}$.

We set the input parameters in Algorithm 1 as $\texttt{VTOL} = 10^{-4}$, $\texttt{MESHTOL} = 10^{-2}$, $\texttt{TOL} = 10^{-2}$, $\texttt{nADAPT} = 50$, $\texttt{nMIN} = 10$.

In Figure 12 and 13, we observe that the qualitative behavior of the fracture is similar to Figure 13 in [24]. Moreover, decreasing ε, the fracture thickness becomes thinner, as expected, and the required number of mesh elements increases (about 7800 for $\varepsilon = 0.06$ and 12000 for $\varepsilon = 0.03$). In both cases, the cardinality is significantly lower with respect to the meshes in [24] which consist of about 20000 mesh elements. In Figure 14, we show a detail of the mesh around the crack for both values of ε at $t = T$. For the two choices of ε, the maximum aspect ratio s_K is about 2000.

6 Conclusions

The optimize-while adapt algorithm employed to model brittle fractures is shown to perform effectively both in terms of computational saving (degrees of freedom) and accuracy for anti-plane and plane-strain elasticity benchmarks.

The first test case confirms the consistency of the analysis for the general-

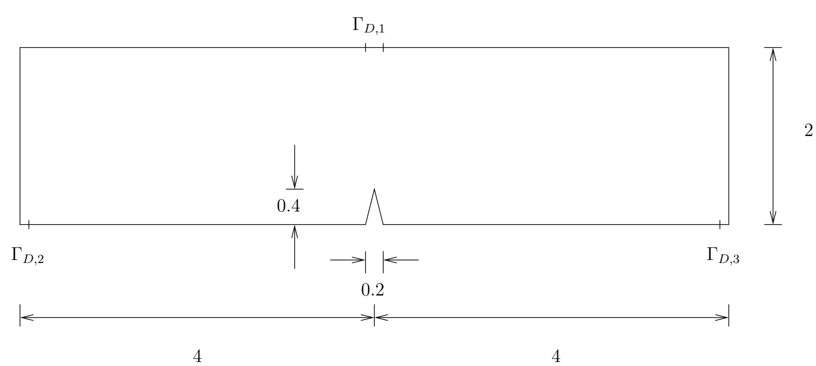

Figure 11: Test Case III : geometric configuration.

(a) $\varepsilon = 0.03$

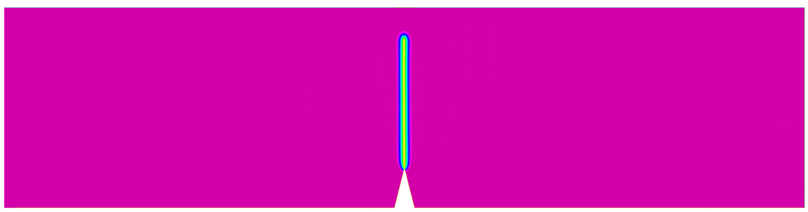

(b) $\varepsilon = 0.06$

Figure 12: Test Case III : v_h-field for different choices of ε.

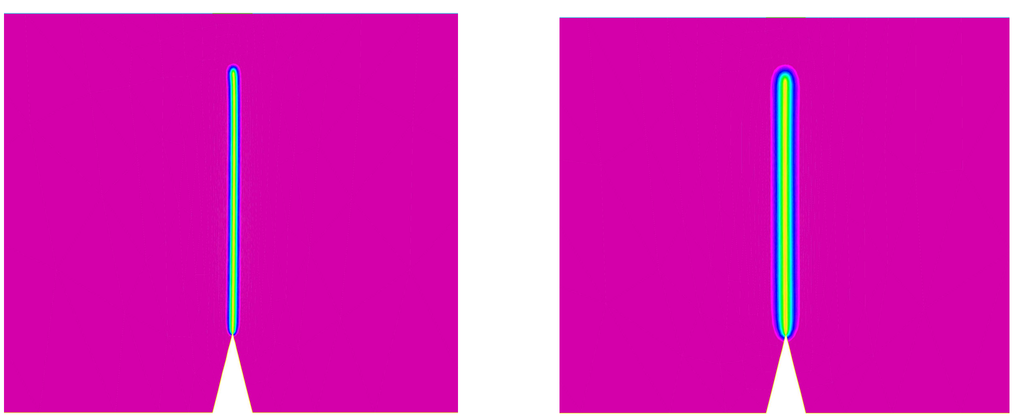

(a) $\varepsilon = 0.03$ (b) $\varepsilon = 0.06$

Figure 13: Test Case III : detail of the v_h-field around the crack path for different choices of ε.

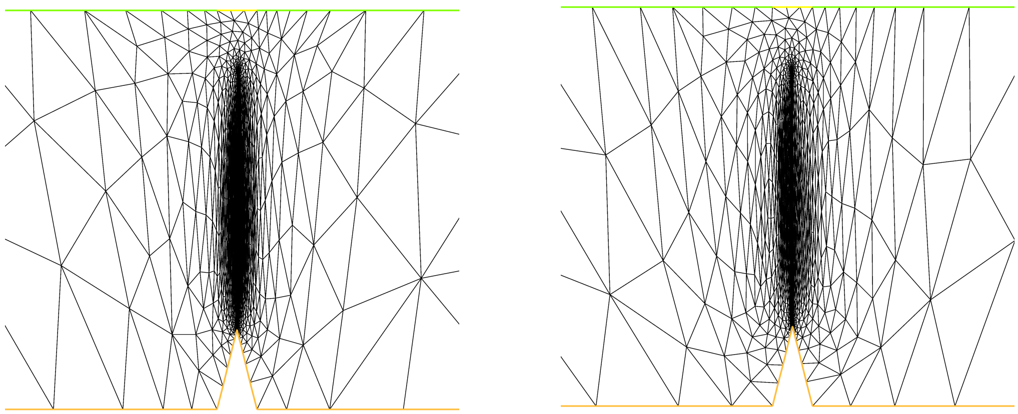

(a) $\varepsilon = 0.03$ (b) $\varepsilon = 0.06$

Figure 14: Test Case III : detail of the anisotropic adapted mesh around the crack path, for different choices of ε.

ized Ambrosio-Tortorelli model with respect to the classical Ambrosio-Tortorelli approximation studied in [4].

The sensitivity analysis to the parameters ε and `TOL`, performed in the second test case, highlights the key-role played by `TOL` in ensuring the correct path tracking. In particular, too high a value of `TOL` fails to detect the expected curved path. The effect of ε seems less strong, at least in the linear case J_{11}, since it affects essentially only the thickness of the fracture.

The plane-strain configuration in the third test case corroborates the effectiveness and accuracy of the whole adaptive procedure compared with the reference literature [24].

As a next step, a comparison with experimental results is clearly advisable to move from verification to validation. A further generalization of the model to include effects due to thermal shocks is also ongoing.

References

[1] L. Ambrosio and V.M. Tortorelli. Approximation of functional depending on jumps by elliptic functional via Γ-convergence. *Commun. Pur. Appl. Math.*, 43(8):999–1036, 1990.

[2] L. Ambrosio and V.M. Tortorelli. On the approximation of free discontinuity problems. *Boll. Unione Mat. Ital. B(7)*, 6:105–123, 1992.

[3] M. Artina, M. Fornasier, S. Micheletti, and S. Perotto. Anisotropic adaptive meshes for brittle fractures: parameter sensitivity. In A. Abdulle, S. De-

paris, D. Kressner, F. Nobile, and M. Picasso, editors, *Numerical Mathematics and Advanced Applications*, pages 293–302. Springer-Verlag, Berlin Heidelberg, Germany, 2014.

[4] M. Artina, M. Fornasier, S. Micheletti, and S. Perotto. The benefits of anisotropic mesh adaptation for brittle fractures under plane-strain conditions. In S. Perotto and L. Formaggia, editors, *New Challenges in Grid Generation and Adaptivity for Scientific Computing*, pages 43–67. SEMA SIMAI Springer, Milano, Italy, 2014.

[5] M. Artina, M. Fornasier, S. Micheletti, and S. Perotto. Anisotropic mesh adaptation for crack detection in brittle materials. *SIAM J. Sci. Comput.*, 37(4):B633–B659, 2015.

[6] B. Bourdin, G.A. Francfort, and J-J. Marigo. Numerical experiments in revisited brittle fracture. *J. Mech. Phys. Solids*, 48:797–826, 2000.

[7] S. Burke, C. Ortner, and A. Sli. An adaptive finite element approximation of a variational model of brittle fracture. *SIAM J. Numer. Anal.*, 48(3):980–1012, 2010.

[8] S. Burke, C. Ortner, and A. Sli. An adaptive finite element approximation of a generalized Ambrosio-Tortorelli functional. *Math. Models Methods Appl. Sci.*, 23(9):1663–1697, 2013.

[9] Ph. Ciarlet. *The Finite Element Method for Elliptic Problems.* North-Holland, Amsterdam, 1978.

[10] Ph. Clment. Approximation by finite element functions using local regularization. *RAIRO Anal. Numér.*, 2:77–84, 1975.

[11] G. Dal Maso. *An Introduction to* Γ*-Convergence.* Birkhäuser Boston, 1993.

[12] G. Dal Maso, G.A. Francfort, and R. Toader. Quasistatic crack growth in nonlinear elasticity. *Arch. Ration. Mech. Anal.*, 176:165–225, 2005.

[13] G. Dal Maso and R. Toader. A model for the quasi-static growth of brittle fractures: existence and approximation results. *Arch. Ration. Mech. Anal.*, 162:101–135, 2002.

[14] L. Ded, S. Micheletti, and S. Perotto. Anisotropic error control for envirenmental applications. *Appl. Numer. Math.*, 58:1320–1339, 2008.

[15] L. Formaggia and S. Perotto. New anisotropic a priori error estimates. *Numer. Math.*, 89:641–667, 2001.

[16] L. Formaggia and S. Perotto. Anisotropic error estimates for elliptic problems. *Numer. Math.*, 94:67–92, 2003.

[17] G.A. Francfort and C.J. Larsen. Existence and convergence for quasi-static evolution in brittle fracture. *Commun. Pur. Appl. Math.*, 56(10):1465–1500, 2003.

[18] G.A. Francfort and J.-J. Marigo. Revisiting brittle fracture as an energy minimization problem. *J. Mech. Phys. Solids*, 46:1319–1342, 1988.

[19] A. Giacomini. Ambrosio-Tortorelli approximation of quasi-static evolution of brittle fractures. *Calc. Var.*, 22:129–172, 2005.

[20] F. Hecht. New developement in FreeFem++. *J. Numer. Math.*, 20:251–265, 2012.

[21] S. Micheletti and S. Perotto. Reliability and efficiency of an anisotropic Zienkiewicz-Zhu error estimator. *Comput. Methods Appl. Mech. Engrg.*, 195(9):799–835, 2006.

[22] S. Micheletti and S. Perotto. Output functional control for nonlinear equations driven by anisotropic mesh adaption: the Navier-Stokes equations. *SIAM J. Sci. Comput.*, 30:2817–2854, 2008.

[23] S. Micheletti and S. Perotto. The effect of anisotropic mesh adaptation on pde-constrained optimal control problems. *SIAM J. Control Optim.*, 49(4):1793–1828, 2011.

[24] C. Miehe, M. Hofacker, and F. Welschinger. A phase field model for rate-independent crack propagation: robust algorithmic implementation based on operator splits. *Comput. Methods Appl. Mech. Engrg.*, 199:2765–2778, 2010.

[25] A. Wächter and L. T. Biegler. On the implementation of a primal-dual interior point filter line search algorithm for large-scale nonlinear programming. *Math. Program.*, 106(1):25–57, 2006.

[26] O.C. Zienkiewicz and J.Z. Zhu. A simple error estimator and adaptive procedure for practical engineering analysis. *Int. J. Numer. Meth. Engng*, 24(2):337–357, 1987.

[27] O.C. Zienkiewicz and J.Z. Zhu. The superconvergent patch recovery and a posteriori error estimates. Part I: The recovery technique. *Int. J. Numer. Meth. Engng*, 33(7):1331–1364, 1992.

[28] O.C. Zienkiewicz and J.Z. Zhu. The superconvergent patch recovery and a posteriori error estimates. Part II: Error estimates and adaptivity. *Int. J. Numer. Meth. Engng*, 33(7):1365–1382, 1992.

[29] O.C. Zienkiewicz and J.Z. Zhu. The superconvergent patch recovery (SPR) and adaptive finite element refinement. *Comput. Methods Appl. Mech. Engrg.*, 101(1-3):207–224, 1992.

MOX Technical Reports, last issues

Dipartimento di Matematica
Politecnico di Milano, Via Bonardi 9 - 20133 Milano (Italy)

05/2016 Alfio Quarteroni, A.; Lassila, T.; Rossi, S.; Ruiz-Baiera, R.
Integrated Heart - Coupling multiscale and multiphysics models for the simulation of the cardiac function

01/2016 Domanin, M.; Buora, A.; Scardulla, F.; Guerciotti, B.; Forzenigo, L.; Biondetti, P.; Vergara, C.
Computational fluid-dynamic analysis of carotid bifurcations after endarterectomy: closure with patch graft versus direct suture

02/2016 Crivellaro, A.; Perotto, S.; Zonca, S.
Reconstruction of 3D scattered data via radial basis functions by efficient and robust techniques

03/2016 Tarabelloni, N.; Ieva, F.
On Data Robustification in Functional Data Analysis

04/2016 Pettinati, V.; Ambrosi, D; Ciarletta P.; Pezzuto S.
Finite element simulations of the active stress in the imaginal disc of the Drosophila Melanogaster

63/2015 Lancellotti, R.M.; Vergara, C.; Valdettaro, L.; Bose, S.; Quarteroni, A.
Large Eddy Simulations for blood fluid-dynamics in real stenotic carotids

62/2015 Signorini, M.; Zlotnik, S.; Díez, P.
Proper Generalized Decomposition solution of the parameterized Helmholtz problem: application to inverse geophysical problems.

61/2015 Tagliabue, A.; Dedè, L.; Quarteroni, A.
Fluid dynamics of an idealized left ventricle: the extended Nitsche's method for the treatment of heart valves as mixed time varying boundary conditions

59/2015 Menafoglio, A.; Guadagnini, A.; Secchi, P.
Stochastic Simulation of Soil Particle-Size Curves in Heterogeneous Aquifer Systems through a Bayes space approach

60/2015 Perotto, S.; Reali, A.; Rusconi, P.; Veneziani, A.
HIGAMod: A Hierarchical IsoGeometric Approach for MODel reduction in curved pipes